Point-source moment tensor inversion via a Bayesian hierarchical inversion with 2D-structure uncertainty: Implications for the 2009-2017 DPRK nuclear tests

Jinyin Hu[1], Thanh-Son Phạm[1] and Hrvoje Tkalčić[1]

[1]Research School of Earth Sciences, The Australian National University, Canberra, ACT, Australia

Corresponding author: Jinyin Hu (jinyin.hu@anu.edu.au)

Key Points:

- A new seismic moment tensor inversion with Bayesian approach incorporates 2D structural uncertainty along specific source-station paths.
- Effective affine-invariant ensemble samplers mitigate the ISO-CLVD tradeoff that impedes resolving shallow explosive sources.
- The newly developed inversion method reveals similar explosive-source mechanisms of five DPRK underground nuclear explosions.

Abstract

Determining the seismic moment tensors (MT) from the observed waveforms, known as full-waveform seismic MT inversion, remains challenging for small to moderate-size earthquakes at regional scales. Firstly, there is an intrinsic difficulty due to a tradeoff between the isotropic (ISO) and compensated linear vector dipole (CLVD) components of MT that impedes resolving shallow explosive sources, e.g., underground nuclear explosions. It is caused by the similarity of long-period waveforms radiated by ISO and CLVD at regional distances. Secondly, regional scales usually bear complex geologic structures; thus, inaccurate knowledge of Earth's structure should be considered a theoretical error in the MT inversion. However, this has been a challenging problem. So far, only the uncertainty of the 1D Earth model (1D structural error), apart from data errors, has been explored in the source studies. Here, we utilize a hierarchical Bayesian MT inversion to address the above problems. Our approach takes advantage of affine-invariant ensemble samplers to explore the ISO-CLVD tradeoff space thoroughly and effectively. Furthermore, we invert for station-specific time shifts to treat the structural errors along specific source-station paths (2D structural errors). We present synthetic experiments demonstrating the method's advantage in resolving the ISO components. The application to nuclear explosions conducted by the Democratic People's Republic of Korea (DPRK) shows highly similar source mechanisms, dominated by a high ISO, significant CLVD components, and a small DC component. The recovered station-specific time shifts from the nuclear explosions present a consistent pattern, which agrees well with the geological setting surrounding the event location.

Plain Language Summary

The seismic sources, including underground faulting, volcanic processes, and manufactured underground explosions, can be represented by a point-source moment tensor (MT), which is an equivalent force system at a point in space and time. Inferring the seismic MT from the observed seismic waveforms is an MT inverse problem. This study designs a new Bayesian inference method to solve this inverse problem by considering two challenging issues: (a) estimating the uncertainty for theory error due to the assumption of 1D Earth's model for the true 3D Earth, and (b) mitigating the theoretical tradeoff between nondouble couple source types at a shallow depth. Here, we determine the MTs of five underground nuclear explosions conducted by the Democratic People's Republic of Korea (DPRK) by fixing their sources at a realistic burial depth of 0.5 km. The robustness of these MT solutions is demonstrated through a series of simulation experiments. Comparisons with previous studies reveal a typical explosive nature of the manmade seismic sources. The recovered theory error is consistent among five explosions, providing a meaningful interpretation of the regional geological setting.

1 Introduction

The seismic moment tensor (MT, a symmetric 3×3 matrix) is a generalized mathematical representation for various seismic sources, including tectonic earthquakes and non-tectonic events, such as manufactured underground explosions and volcanic processes, including eruptions. The point source assumption must hold to use MT, which is generally valid for small-to-medium-size earthquakes (Aki & Richards, 2002). The seismic MT introduces source components beyond a double-couple (DC) force system, which only describes slip on a planar fault (Gilbert, 1971). One convenient way is to decompose an MT into double-couple (DC) and

non-double-couple (NDC) components consisting of isotropic (ISO) and compensated linear vector dipole (CLVD) components, which was proposed by Knopoff and Randall (1970), then further developed by others (e.g., Jost & Herrmann, 1989; Julian et al., 1998; Sipkin, 1986; Vavryčuk, 2015). This decomposition of MT has specific physical properties. DC part depicts the shear faulting, which is the focal mechanism of most tectonic earthquakes. The ISO represents the explosion/collapse and involves volumetric changes. Even though an MT only including a pure CLVD does not correspond to any simple seismic sources, its combination with ISO can explain the tensile or compressive faulting (Vavryčuk, 2001, 2011, 2015). Besides, shear faulting on a non-planar fault can be represented by the combination of DC and CLVD, referred to as deviatoric MT, assuming zero ISO. A ring fault was proposed to explain the teleseismic and regional long-period waveforms of the 1996 Bárðarbunga earthquake (e.g., Konstantinou et al., 2003; Nettles & Ekström, 1998; Tkalčić et al., 2009).

The NDC sources have been found in various geologic settings. At the early stage of seismology, some minor departures from the DC mechanism were considered artifacts of the inversion, e.g., data noise or theory error. As the instruments and methods are developed, the NDC components are confirmed to correspond to the source processes. They are found in various geological settings but are most common in volcanic environments (e.g., Dreger et al., 2000; Duputel & Rivera, 2019; Julian, 1983; Mustać & Tkalčić, 2016; Nettles & Ekström, 1998; Saraò et al., 2001; Tkalčić et al., 2009), and geothermal environments (e.g., Johnson, 2014; Martínez-Garzón et al., 2017; Mustać et al., 2018; Mustać & Tkalčić, 2017; Ross et al., 1996), and underground explosions (e.g., Alvizuri et al., 2018; Chiang et al., 2014; Dreger et al., 2021; Ford et al., 2009; Mustać et al., 2020). Julian et al. (1998) and Miller et al. (1998) comprehensively reviewed the NDC sources in theory and applications. The relative significance of the NDC component is a critical indicator in discriminating between tectonic earthquakes and non-tectonic events (e.g., volcanic or explosive events). Therefore, the resolvability of MT, especially the NDC components, plays an essential role in seismic source studies, which relies on the seismic MT inversion.

Utilizing seismological observations to determine the MT comprises a recurring and broad central theme of modern seismology, which refers to seismic MT inversion. There are four groups of MT inversion methods based on the used observations. The first group of MT inversion uses the P-wave first motion polarities recorded at various directions to determine the fault geometry, i.e., the focal mechanism (e.g., Dillinger et al., 1972; Eaton & Mahani, 2015; Hardebeck, 2002; Julian, 1986; Reasenberg & Oppenheimer, 1985). The second group fits P- and S-wave amplitude or their ratio. For example, the absolute P and S amplitudes were used by Ebel and Bonjer (1990), Rögnvaldsson and Slunga (1993), and Stanek et al. (2014). The third group of MT inversion uses hybrids of various observations, including the first-motion polarity and amplitude ratios (e.g., Julian & Foulger, 1996; Shang & Tkalčić, 2020). The fourth group takes advantage of the full waveforms, which contain much more information than the body-wave polarity and amplitude ratio. However, it can be readily applied only to M_W>4.0 earthquakes. Based on the different implementations, it is divided into two main categories: The time-domain full-waveform MT inversion (e.g., Dreger et al., 2000; Dziewonski et al., 1981; Minson & Dreger, 2008; Pasyanos et al., 1996; Romanowicz et al., 1993), and the frequency-domain full-waveform MT inversion (e.g., Cesca et al., 2006; Dahm et al., 1999; Nakano et al., 2008; Romanowicz, 1982; Stump & Johnson, 1977). Cesca et al. (2010) and Vavryčuk and Kühnv (2012) combined the time and frequency domain inversions. Future discussions about the

advantages and disadvantages of each method and their categories can be found in Shang and Tkalčić (2020).

Rigorous uncertainty estimate has been one of the frontiers in seismic MT inversion. A complete uncertainty treatment should consider both data noise mainly involved in the data acquisition/processing and theoretical error primarily caused by the imperfect knowledge of Earth's structure (i.e., structural error). Data noise has been estimated with different noise models, such as a Gaussian or an exponentially decaying noise model (e.g., Bodin et al., 2012; Duputel et al., 2012), empirical noise model from data residuals (e.g., Dettmer et al., 2007; Mustać et al., 2020), from synthetic noise series (e.g., Gouveia & Scales, 1998; Piana Agostinetti & Malinverno, 2010; Sambridge, 1999), or model with approximating the pre-event ambient noise with two-attenuated cosine functions (Mustać et al., 2018; Mustać & Tkalčić, 2016). Incorporating structural uncertainty has been conducted in the case of 1D Earth's structure by assuming a Gaussian noise distribution for teleseismic Green's functions (Yagi & Fukahata, 2011), by estimating a covariance matrix from linear perturbation of Green's functions (Duputel et al., 2014), or evaluating a covariance matrix from synthetically generated Green's functions with randomly perturbed Earth's models (e.g., Hallo & Gallovič, 2016). These studies made remarkable efforts to handle data noise and theoretical error separately. Recent advancements treating data noise and theoretical errors jointly have been made. Vasyura-Bathke et al. (2021) analyzed different combinations of covariance matrixes for data noise and structural uncertainty. Phạm and Tkalčić (2021) constructed a combined covariance matrix for data noise and structural error. Namely, an explicit covariance matrix of structural error is obtained by the Monte Carlo method from linear perturbations of the 1D-Earth model. These works provide a pathway to estimating 1D structural error considering the overall structural effect averaged for all stations.

Constraining the source parameters better relies on possessing the accurate Earth structure model. The MT inversion using the 1D Earth model has earned many successes by using long-period waveforms, which are not sensitive to the small-size 3D heterogeneity (e.g., Dziewonski et al., 1981; Ekström et al., 2012). Moreover, the MT inversion has been advanced further by incorporating the 1D Earth structural uncertainty, as discussed above. At the same time, we recognize that an accurate knowledge of 3D anisotropic, heterogeneous Earth would constrain source parameters significantly better. Multiple studies have addressed this issue, concluding that the 3D Earth model can improve the source resolvability (e.g., Donner et al., 2020; Fichtner & Tkalčić, 2010; Gallovič et al., 2010; Hejrani et al., 2017; Hingee et al., 2011; Kim et al., 2011; Wang & Zhan, 2020). However, due to high computational demand, treating uncertainty from the imperfection of 3D Earth structures (3D structural error) remains challenging. Therefore, in this study, we explore a transitional solution before progressing the uncertainty quantification from 1D to 3D structural errors.

Apart from the above aspect, an inherent ambiguity of the NDC components exists in seismic source inversion for shallow sources. The resolvability of MT becomes more difficult as the point-source focus becomes shallower (Dziewonski et al., 1981; Kanamori & Given, 1982; Kawakatsu, 1996). Hejrani & Tkalčić (2020) analyzed two main challenges in conjunction with the shallow-source inversion: an unbalanced range of amplitudes from a vertical dip-slip mechanism in various frequency bands and the tradeoff between ISO and CLVD. They addressed the first problem by utilizing high-frequency waveforms (>0.025 Hz), a possible approach for a relatively simple geologic setting. However, the intrinsic difficulty in analyzing shallow explosive sources such as underground nuclear explosions remains due to the similarity

of long-period waveforms at regional distances. Unless short periods (high frequencies) can be utilized, many different MTs can fit the regional observed waveforms equally well, leading to considerable uncertainty in MT solutions. Even though the problem can be mitigated by extra constraints such as adding the first motion polarities of the teleseismic P-waves (e.g., Chiang et al., 2014; Dreger et al., 2021; Ford et al., 2012), there is still an urgent need for advanced inversion algorithms to avoid the local optimal solution traps and explore the solution space thoroughly.

In this study, we develop an MT inversion within a hierarchical Bayesian framework to address the abovementioned problems. Tkalčić et al. (2009) and Hallo & Gallovič (2016) noted that the significant source of long-period Green's functions uncertainty is due to the misalignment between predicted waveforms and observations when using a 1D layered model to present the medium between the source and receivers. Therefore, we propose a scheme to treat the structural error along specific source-station paths when assuming a 1D Earth model (i.e., 2D structural error) as a transition from 1D structural error to 3D structural error, which uses station-specific time shifts between the observed and predicted waveforms. The station-specific time shifts are set as free parameters and determined simultaneously with MT parameters during the inversion, which is the hierarchical aspect of the inversion problem. Treating the time shifts as a part of the inversion is different from the widely used practices, where a grid search with repeating inversions usually determines time shifts (e.g., Mustać et al., 2020), or cross-correlations match the synthetics with observed waveforms (e.g., Alvizuri et al., 2018; Dreger et al., 2021).

Secondly, to mitigate the ISO-CLVD tradeoff, we apply an advanced sampling algorithm for Bayesian MT inversion to explore the parameter space thoroughly and effectively. This sampling method is named "effective affine-invariant ensemble samplers" and was proposed by Goodman & Weare (2010) and well implemented with Python (Foreman-Mackey et al., 2013). The ensemble samplers work simultaneously and efficiently to sample the posterior distribution of the parameter model, compared with other traditional sampling algorithms such as the Metropolis-Hastings algorithm (MHA, Hastings, 1970; Metropolis et al., 1953), which applies only one sampler. Its performance is not strongly affected by the linear dependence between MT parameters caused by the ISO-CLVD tradeoff, which makes it more suitable for MT inversion for shallow seismic events.

The rest of the paper is as follows. In section 2, we introduce the methodology development of the proposed hierarchical Bayesian MT inversion framework, i.e., 2D structural error treated by the station-specific time shift and the advanced sampling method with effective affine-invariant ensemble samplers. In section 3, we conduct synthetic experiments using an actual configuration of a shallow underground explosion and stations to demonstrate the feasibility of our method. Section 4 is the application to five underground nuclear explosions conducted by the Democratic People's Republic of Korea (DPRK). Finally, in sections 5 and 6, we discuss the MT solutions for real data applications and compare them with previous studies. A brief conclusion is presented at the end.

2 Methodology

2.1 Forward modeling of waveforms

In the point-source assumption, the synthetic displacement on the Earth's surface can be expressed as a linear combination of Green's functions (GFs). By following the method developed initially by Jost and Hermann (1989), then improved by Minson and Dreger (2008), the displacement of data samples in the direction at a seismic station is written as

$$g_i(\mathbf{m}) = \mathbf{G}_i\mathbf{m}, \tag{1}$$

where $\mathbf{G}_i \in \mathbf{R}^{N\times 6}$ is the six-component GFs for a given Earth's structure model, $\mathbf{m} \in \mathbf{R}^6$ is the seismic MT. This will hold when the source location and origin time are known precisely. This is a reasonable assumption for manmade seismic sources such as nuclear explosions. The specific expressions of synthetic displacements, $g_i(\mathbf{m})$ in vertical, radial, and tangential directions for a full MT, $\mathbf{m} = \left[M_{xx}, M_{yy}, M_{zz}, M_{xy}, M_{xz}, M_{yz}\right]^T$, can be found in Minson and Dreger (2008).

2.2 Bayesian MT inference

The MT can be inferred from the observed seismograms because each synthetic $g_i(\mathbf{m})$ corresponds to an observed seismogram d_i. The Bayesian approach is one of the most powerful inversion methods because it can explore the solution space thoroughly by using appropriate samplers and generates an ensemble of solutions instead of only an optimal solution. The spread of the sampled solutions quantifies solution uncertainty.

The MT parameters are treated as random variables in Bayes' theorem (Bayes & Price, 1763), and its posterior distribution can be derived through a likelihood function. The posterior probability of MT parameters $\mathbf{m}$ given the observation $\mathbf{d} \coloneqq \{d_i\}$, based on the likelihood function $p(\mathbf{d}|\mathbf{m})$, a prior distribution $p(\mathbf{m})$, and the evidence of the data $p(\mathbf{d})$, is given as

$$p(\mathbf{m}|\mathbf{d}) = \frac{p(\mathbf{d}|\mathbf{m})p(\mathbf{m})}{p(\mathbf{d})} \tag{2}$$

We assume an uninformative prior, $p(\mathbf{m}) = c$, and the evidence $p(\mathbf{d})$ is also an unknown constant. These two constants, $p(\mathbf{m})$ and $p(\mathbf{d})$, can be omitted without affecting the posterior distribution's relative landscape but ensuring the algorithm's efficiency. Consequently, the likelihood function $p(\mathbf{d}|\mathbf{m})$ is used as the posterior probability $p(\mathbf{m}|\mathbf{d})$ in this study. The posterior probability can be numerically estimated by coordinate distributions obtained by a Markov chain Monte Carlo (McMC) sampling method (Sambridge & Mosegaard, 2002).

The likelihood function includes all information from the data and Earth's structures for the Bayesian inversion. The widely-used likelihood function has a Gaussian distribution (e.g., Dettmer et al., 2007; Duputel et al., 2012; Mustać & Tkalčić, 2016; Phạm & Tkalčić, 2021; Sambridge et al., 2006)

$$p(d_i|\mathbf{m}) = \frac{1}{\sqrt{(2\pi)^N|C_i|}} exp\left(-\frac{1}{2}(g_i(\mathbf{m}) - d_i)^T C_i^{-1}(g_i(\mathbf{m}) - d_i)\right), \tag{3}$$

C_i and $|C_i|$ are uncertainty covariance matrix and its determinant. The subscript *i* denote an individual seismogram component in the observed data. We assume stochastically independent

observed components of all stations so that the aggregated likelihood function for $M = n_s \times 3$ (n_s is the number of three-component stations) component seismograms is

$$p(\mathbf{d}|\mathbf{m}) = \prod_{i=1}^{M} \frac{1}{\sqrt{(2\pi)^N |C_i|}} exp\left(-\frac{1}{2}(g_i(\mathbf{m}) - d_i)^T C_i^{-1}(g_i(\mathbf{m}) - d_i)\right). \quad (4)$$

It measures the overall waveform fit level between the observed and the predicted seismograms, which makes it a critical factor in Bayesian seismic source inversion.

2.3 Estimating the covariance matrix

The covariance matrix C_i in Equation 4 enables the consideration of various sources of uncertainty in the inversion problem. There are two sources of uncertainty: data noise, the empirical theory error, or their combination. Firstly, data noise is mainly caused by background ambient noise at the recording site and instrumental noise in the data acquisition. Secondly, the theory uncertainties, or uncertainties relating to the forward problem, are any source of errors due to theoretical approximations in the forward problem. It is reasonable to assume that the most significant contribution to the theory error is due to our imperfect knowledge of the Earth's interior structure, also referred to as structural uncertainty in this study.

To thoroughly consider the uncertainty in an MT inversion problem, the covariance matrix should account for both sources of uncertainties. Therefore, a combined covariance matrix was proposed by Tarantola & Valette (1982) and further explored by other studies (e.g., Duputel et al., 2012; Phạm & Tkalčić, 2021; Tarantola, 2005; Vasyura-Bathke et al., 2021), which is written as

$$C_i = C_i^d + C_i^t, \quad (5)$$

where C_i^d and C_i^t are covariance matrices for the data noise and structural error, respectively. The structural covariance matrix, C_i^t, is estimated empirically by perturbating a 1D Earth model using the Monte-Carlo simulation. Moreover, Duputel et al. (2012) and Phạm & Tkalčić (2021) demonstrated the dependency of C_i^t on a prior MT, i.e., $C_i^t(m)$, which is computationally expensive, especially when 3D Earth is considered. Furthermore, the empirical estimation of the structural covariance matrix requires subjective choices for scale and parameterization of the Earth model perturbations, which are currently subjected to future research.

Here, we propose a simplified treatment of the structural uncertainty to avoid the expensive Monte-Carlo simulation, in which the structural errors are treated using station-specific time shifts (more details to be considered in Section 2.4). The covariance matrix C_i from Equation 4 only includes uncertainty from data noise. In further simplification, data noise on each component is assumed to be uncorrelated when signal-to-noise ratios (SNR) of inverted waveforms are large, which is usually the case for intermediate-large earthquakes. The covariance matrix C_i becomes diagonal

$$C_i = \sigma_i^2 \mathbf{I}, \quad (6)$$

where σ_i^2 is the unknown noise variance of each seismogram. To reduce the number of noise parameters and avoid the wide range to search for them, we follow the approach proposed by Phạm & Tkalčić (2021) to parameterize the covariance matrix in Equation 6 as,

$$C_i = h \cdot \left(\sigma_i^{ref}\right)^2 \mathbf{I}, \quad (7)$$

where σ_i^{ref} is the reference noise strength for each component that is the pre-computed standard deviation of the 1-hour pre-event ambient noise of three components at each station, and h is the station-specific noise hyper-parameter. The pre-event noise used to calculate covariance matrix is pre-processed in the same way as the data used in the inversion.

2.4 Accounting for 2D Earth's model uncertainty by station-specific time shifts

This study provides a simplified scheme to treat the 2D structural error, i.e., structural error along specific source-station paths, by inverting for the station-specific time shifts between predicted waveforms and observations. To demonstrate the validity of this simplification, we take the DPRK2017 explosion as an example to indicate the misalignment between waveforms from perturbated 1D Earth models. As Figure 1b shows, a four-layer velocity model (MDJ2, Ford et al., 2009) is randomly perturbated 300 times given 5% uncertainty (see Pham & Tkalčić, 2021 for the description of 1D model perturbation). An ensemble of waveforms generated by the same explosive MT in these perturbated 1D models is plotted in Figure 1c. The waveforms at the same station feature a high degree of similarity in long period band, e.g., 20 – 50 s, used in this study. At stations MDJ, INCN, and TJN, these 300 waveforms of each component almost overlap, showing insignificant misalignments in phase and amplitude. However, the misalignments in phase (referred to as time shift) become more apparent and more significant as the epicenter distance increases at the other four stations while the amplitudes remain similar.

The high order of similarity after waveform alignment confirms the dominance of time shifts by the model uncertainty in 1D. Specifically, we performed a grid search for the time shift at each component to achieve the best waveform fit (i.e., the highest variance reduction, VR, defined in Equation S17b of Phạm & Tkalčić, 2021) between the waveforms from the MDJ2 model (red in Figure 1b) and the perturbated MDJ2 model (gray in Figure 1b). The re-aligned waveforms are shown in Figure 1d. The overall VR of waveform fit is 95.8% after realignment. Therefore, time shifts dominate the structural error within 5% perturbation uncertainty, providing a pathway to treat the primary source of the uncertainty from structural errors. Hallo & Gallovič (2016) derived an approximate covariance matrix by considering these random time shifts in waveforms. In this study, alternatively, we directly invert the station-specific time shifts simultaneously with MT parameters, which sets the station-specific time shifts as free parameters determined by the data to account for the structural error along specific wave propagation paths.

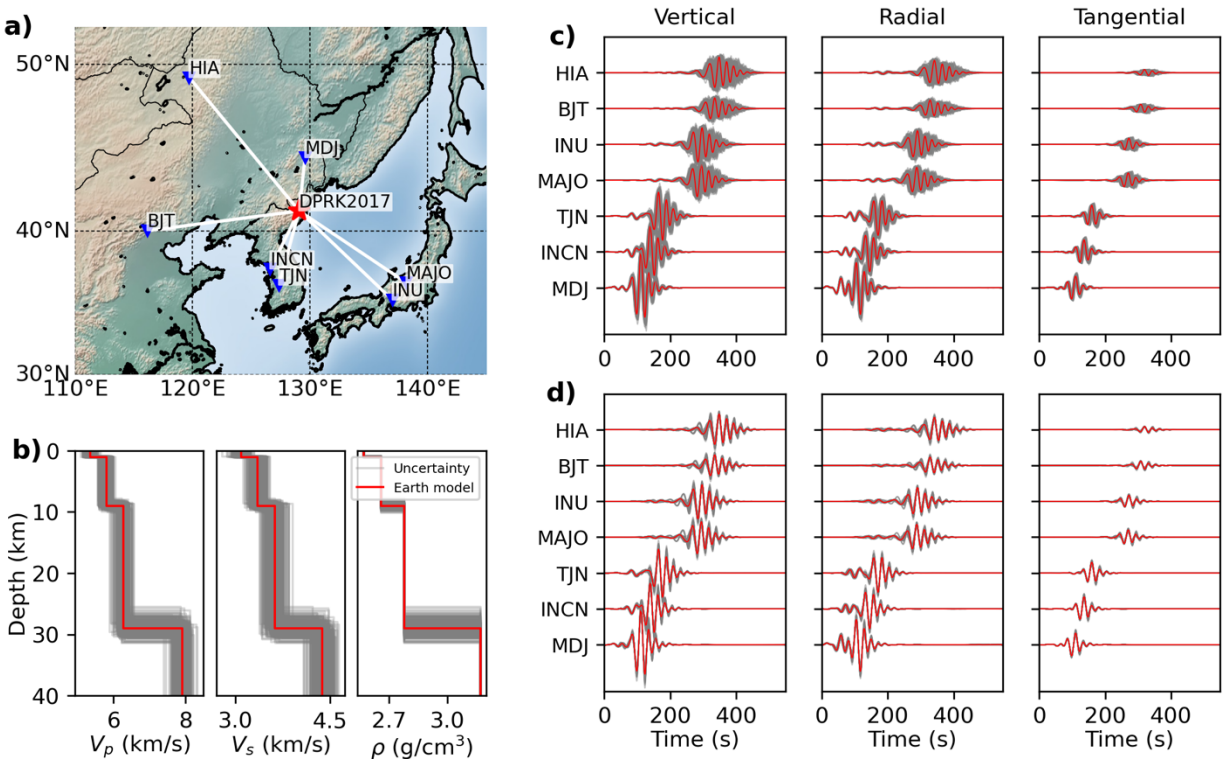

Figure 1. Synthetic scenario to demonstrate the time shifts generated by perturbated 1D velocity models. (a) Map showing the DPRK2017 explosion location (red star) and seven seismic stations (blue triangles). (b) The P-wave and S-wave velocity and density of the MDJ2 model (red), which is a four-layer velocity model (Ford et al., 2009), and its 300 perturbed structures (gray) given 5% uncertainty. (c) The three-component waveforms for perturbed 1D Earth structures in (b) and the MT of DPRK2017 explosion from Alvizuri and Tape (2018). All waveforms are filtered using 20–50 s period band. (d) The re-aligned waveforms from (c) by grid search for the optimal time shift at each component to obtain the best variance reduction (i.e., 95.8%).

Allowing noise amplitudes and time shifts, i.e., the hierarchical aspect of Bayesian inference, makes the MT inversion non-linear. The noise parameters are already included in the Bayesian inversion through the likelihood function in Equations 4 and 7. The time-shifting of a waveform can be described analytically as,

$$g_i'(\mathbf{m}) = F^{-1}\left[F[g_i(\mathbf{m})] \cdot e^{-i\omega\tau}\right], \tag{8}$$

in which F, F^{-1} denote forward and inverse Fourier transformation, respectively. τ is the station-specific time-shift parameter, which allows continuous time-shifting values rather than being restricted by discrete sampling intervals. In this work, the τ is bounded by $[-10, 10]$ to avoid cycle skipping for waveforms filtered between 20 - 50 s, which is the frequency band we used in this study. Therefore, the complete parameter model to invert for is defined as $[\mathbf{m},\ \mathbf{h},\ \boldsymbol{\tau}]$ where $\mathbf{m} = \left[M_{xx}, M_{yy}, M_{zz}, M_{xy}, M_{xz}, M_{yz}\right]^T$ parameterizes a full MT, $\mathbf{h} = \left[h_1, h_2 \cdots h_{n_s}\right]$ parameterizes station-specific data noise strengths, and $\boldsymbol{\tau} = \left[\tau_1, \tau_2 \cdots \tau_{n_s}\right]$ are the station-specific time shifts. Finally, the likelihood function in Equation 4 is rewritten as

$$p(\mathbf{d}|\mathbf{m},\mathbf{h},\boldsymbol{\tau}) = \prod_{i=1}^{M} \frac{1}{\sqrt{(2\pi)^N |C_i|}} exp\left(-\frac{1}{2}(g_i'(\mathbf{m}) - d_i)^T C_i^{-1}(g_i'(\mathbf{m}) - d_i)\right). \quad (9)$$

312

313 2.5 Exploring the parameter space using affine-invariant ensemble samplers

314 The inherent ambiguity between pure ISO and vertical CLVD is a significant challenge in
315 MT inversion for shallow seismic sources using long-period regional waveforms. At the shallow
316 depths, seismic waveforms recorded by regional stations (< 1200 km) are dominated by surface
317 waves, which have minimal sensitivities to the vertical force couple. This explains the high
318 similarity between waveforms in Figure 2c generated by various ISO-dominating and vertical-
319 CLVD-dominating sources in Figure 2a at 0.5 km depth, which is meant to reproduce the
320 comparison by Kawakatsu (1996). The waveform similarity leads to the severe tradeoff between
321 ISO and CLVD when resolving for NDC components of the shallow sources, e.g., manmade
322 underground explosions. In parameter space, this ISO-CLVD tradeoff presents a strong linear
323 dependence among three diagonal elements of an MT, i.e., M_{xx}, M_{yy}, and M_{zz}, as shown in
324 Figures 2b. It is challenging to thoroughly sample this type of parameter distribution in Bayesian
325 MT inversion using sampling algorithms such as the Metropolis-Hastings algorithm (MHA,
326 Hastings, 1970; Metropolis et al., 1953). Here, we promote using the affine-invariant ensemble
327 samplers (Goodman & Weare, 2010) for this MT inverse problem to effectively sample the MT
328 solution spaces to mitigate the challenge caused by the shallow source depths.

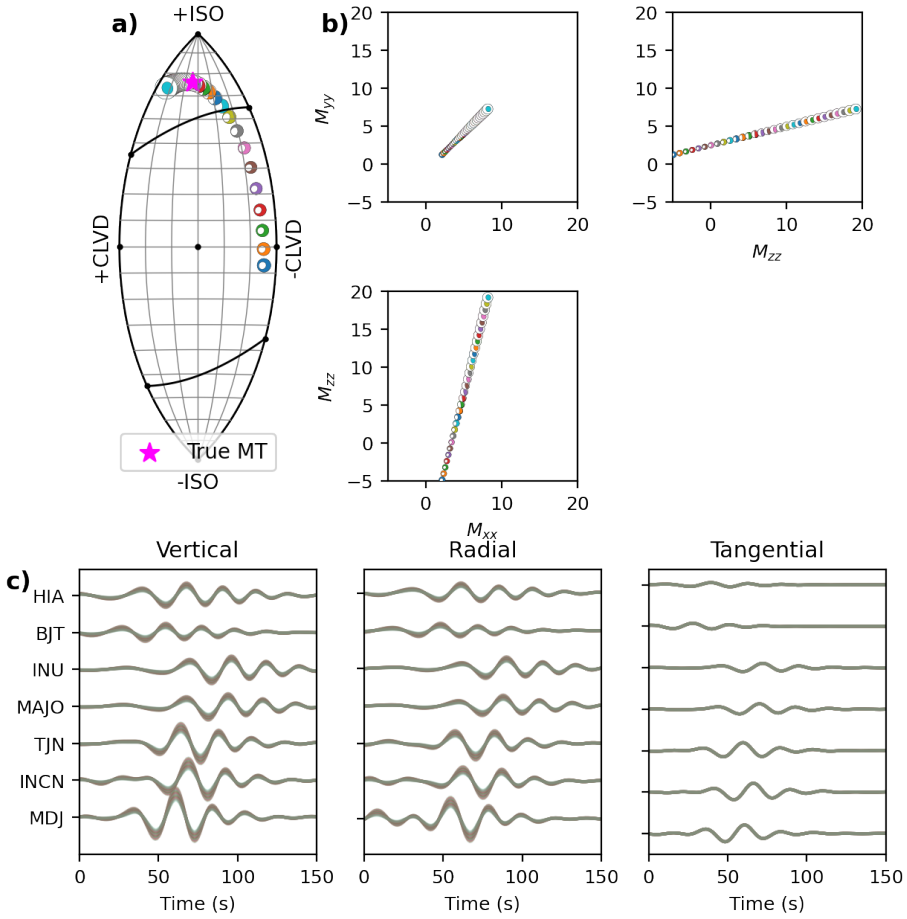

Figure 2. The ambiguity of non-double-couple components of the shallow seismic source. (a) Various inverted seismic MTs (shown as focal mechanisms in different colors) yield almost identical seismic waveforms. The magenta star is the input MT from Alvizuri and Tape (2018). (b) The linear relationship between three pairs of MT parameters, i.e., M_{xx} and M_{yy}, M_{xx} and M_{zz}, and M_{yy} and M_{zz}. (c) The synthetic three-component waveforms at seven stations (Figure 1a) produced by the MTs shown in (a).

This approach of ensemble samplers employs K walkers in a coordinated manner by exchanging their current coordinates to explore the N-dimensional unknown model space. Goodman & Weare (2010) proposed the 'stretch move' proposal scheme, in which the next move of a walker $\mathbf{m}_i$ is proposed in two steps, as in Figure 3. First, a random partner is chosen from the complementary walkers in the ensemble, say $\mathbf{m}_j$. Then, the proposed move is drawn randomly along the line connecting the two walkers,

$$\mathbf{m}_i' = \mathbf{m}_j + Z \cdot (\mathbf{m}_i - \mathbf{m}_j). \tag{10}$$

In Equation 10, Z is a random, positive number drawn from a probability distribution $g(z)$ in the $[1/a, a]$ interval,

$$g(z) \propto \begin{cases} \frac{1}{\sqrt{z}} & \text{if } z \in \left[\frac{1}{a}, a\right], \\ 0 & \text{otherwise} \end{cases} \tag{11}$$

The parameter a, where $a > 1$, is the only parameter to adjust the performance of the 'stretch move' scheme. Furthermore, $a = 2$ has empirically been found to be an optimal choice in many large-scale inverse problems (Foreman-Mackey et al., 2013; Goodman & Weare, 2010). This proposed move of the walker $\mathbf{m}_i$ is accepted based on a probability involving the probabilities of the current coordinate and the proposed move,

$$q = \min\left(1, Z^{N-1}\frac{p(\mathbf{d}|\mathbf{m}_i')}{p(\mathbf{d}|\mathbf{m}_i)}\right). \tag{12}$$

The stretch move is iterated for other walkers in the ensemble before proceeding to the next iteration. The ensemble samplers are implemented in a lightweight, well-tested Python package, emcee (Foreman-Mackey et al., 2013).

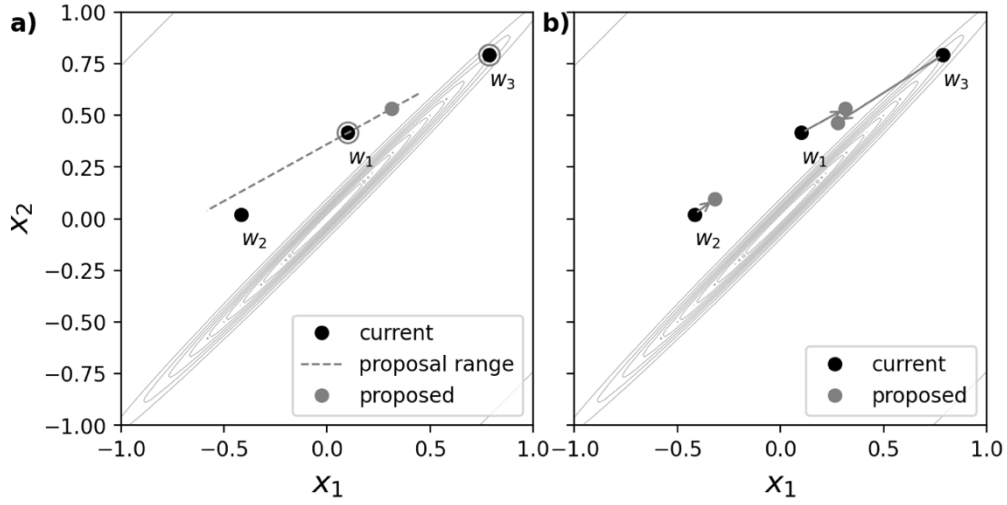

Figure 3. Schematic demonstration in two-dimensional parameter space of the stretched move used in the affine-invariant McMC (Goodman & Weare, 2010). The background shows the contours of the probabilistic distribution to be sampled. In (a), black dots mark the current positions of three walkers. Grey dot is a proposed move for the walker w_1, with a randomly chosen partner w_3. The dashed gray line shows the range of proposals for the next move of w_1. In (b), gray dots are proposed to move all three walkers from their current positions, which will be accepted or rejected randomly.

The ensemble samplers, designed as above, possess the affine invariant property, whose performance is not affected by an affine transformation of the coordinates. Such transformations are often caused by the linear dependence between parameters, which leads to a highly anisotropic probability distribution, as demonstrated in Figure 2b. However, the affine-invariant ensemble samplers can thoroughly and effectively sample this type of distribution compared to traditional sampling algorithms. As the example in Figures 4a and 4b shows, with the same number of sampling steps, i.e., 1000, Gibb's sampler only samples part of the target distribution, while the ensemble samplers of 5 walkers with 200 steps each explore the whole target distribution. This property makes it more suitable for MT inversion for shallow sources. In the following numerical experiments and applications to real data, we will demonstrate the advantages of the ensemble samplers for the MT inversion problem of non-double-couple components in shallow seismic sources.

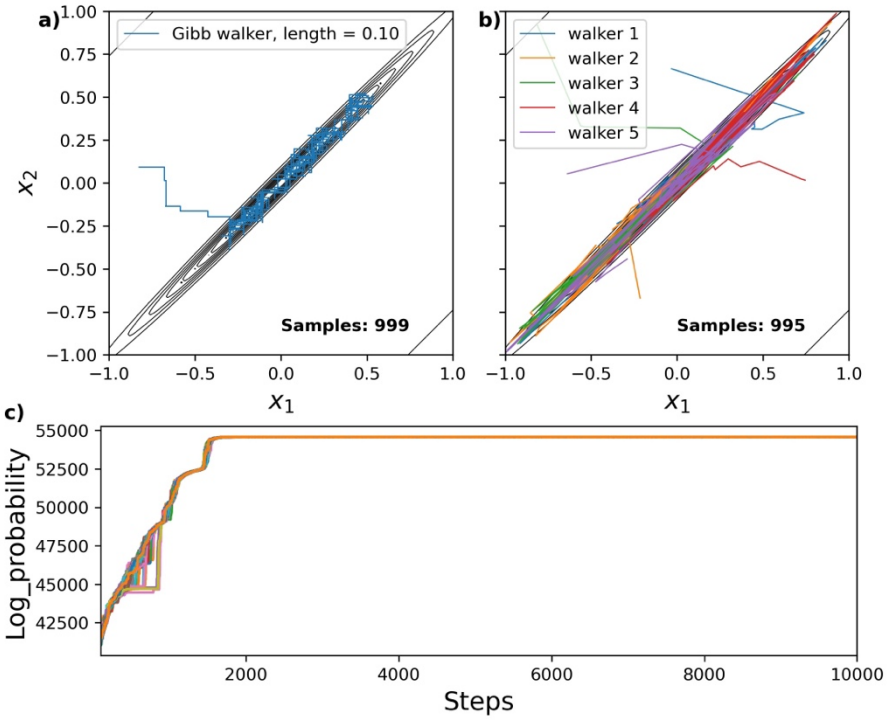

372 **Figure 4.** Comparison of sampling efficacy between (a) the traditional Metropolis-Hasting
373 method and (b) the ensemble samplers with stretched moves (Goodman & Weare, 2010). The
374 background contours show the target probability distribution. Each colored trace represents the
375 trajectory of a walker. There are 1000 random samples drawn in both cases. (c) Posterior
376 probability varying with the inversion step during the proposed Bayesian MT inversion using
377 affine-invariant ensemble samplers. Color-coded lines are for different 512 walkers during
378 10,000 iterations.

379 ## 3 Synthetic Experiment

380 ### 3.1 Experiment configuration

381 We design numerical experiments having a realistic source-receiver configuration to
382 demonstrate the feasibility of this approach on the MT inversion for resolving NDC components
383 of shallow seismic sources. Figure 1 shows the event location and seven stations providing good
384 azimuthal coverage to the interested event located at the DPRK nuclear test site. Epicentral
385 distances from the stations range from 370 km up to 1100 km. The four-layer 1D velocity model
386 MDJ2 (Ford et al., 2009) simulates synthetic waveforms. An explosive event is fixed at 0.5 km
387 depth, and its input MT is the solution of the DPRK2017 event from Alvizuri & Tape (2018),
388 which includes 63.7% ISO, 6.4% CLVD, and 29.8% DC, with a moment magnitude M_w =5.21.

389 The "noisy" synthetic waveforms are calculated with data and structural uncertainties.
390 Noise-free waveforms are band-passed filtered between 20–50 second periods. First, three-
391 component real recorded ambient noise before the origin time of DPRK2017 explosion, pre-
392 processed in the same way as noise-free waveforms, are added to corresponding three-
393 component noise-free waveforms at the sites to represent the data noise. The reference noise

strengths, σ_i^{ref}, are pre-computed from the 1-hour pre-event ambient noise (Equation 7) and the input relative noise levels, $h_1, h_2 \ldots h_7$, are set to unity. Secondly, to introduce the structural uncertainty, we shift the data with station-specific times (Table 1). Waveforms are shifted forward, corresponding to positive time shifts for three stations in China and South Korea, and backward, corresponding to negative time shifts for two stations in Japan. The signs of the shifts simulate the actual difference between the MDJ2 model and slower continental crust toward the western sites and faster oceanic crust toward the eastern sites. The time shifts are the only source of structural uncertainty introduced in synthetic waveforms.

Table 1. True station-specific time shifts (unit: second), used for the numerical experiment of MT inversion for the DPRK2017 test.

Explosion	IC.MDJ	IC.BJT	IC.HIA	IU.INCN	KG.TJN	IU.MAJO	G.INU
DPRK2017	4.0	3.7	4.0	2.0	1.5	-4.5	-5.5

3.2 Inversion results for a synthetic, shallow-source explosion

The affine-invariant ensemble samplers introduced for the seismic MT inversion in this study (Section 2.5) perform excellently in terms of efficiency and effectiveness. We used 512 walkers and 10,000 iterations in all inversions presented in this study. The samples from each walker are not independent. The emcee follows Goodman & Weare (2010) and uses the autocorrelation time τ_f, i.e., the number of steps before producing independent samples of the target distribution, to estimate the effective number of independent samples. Running with a large number of walkers is beneficial to obtain more independent samples and a higher acceptance rate, that is, the fraction of proposed steps to be accepted (Foreman-Mackey et al., 2013; Goodman & Weare, 2010). Finally, the first several times τ_f of samples of each walker are discarded as the burn-in stage. The number of discarded samples is determined via tests prior to the inversion to make sure the remaining samples have reached the convergency, where all walkers fluctuate around the similar highest probability. The samples in the convergency stage are thinned by half the autocorrelation time and flattened across the walkers to obtain the solution ensemble. In this study, we discard the first half of 10,000 iterations of each walker that is about 10 times of the maximum τ_f of all walkers. The remaining half of 10,000 iterations are used as the convergency stage. The probability varying with the inversion step for all walkers is plotted in Figure 4c with different colors. As one can see, in the burn-in stage, the probability from each walker increases quickly before reaching the convergence stage. The inversion takes 4.5 minutes on a personal computer (3.1 GHz 6-Core Intel Core i5) for this numerical experiment.

This proposed Bayesian MT inversion successfully recovers the shallow explosive source using affine-invariant ensemble samplers. The inversion results are summarized in Figures 5, 6 and 7. According to the lune source-type diagram (Tape & Tape, 2012) shown in Figure 5c, the algorithm with ensemble samplers effectively explores the parameter space. Initially, a wide variety of source types is explored (copper dots). Then the samplers go through a stripe in the lune diagram to explore the ISO-CLVD tradeoff with higher posterior probabilities (dark brown dots). The samplers eventually converge to a small area corresponding to the highest posterior

probability (black dots; also plotted in Figure 5b for clarity), where the cyan cross denotes their mean. As can be seen in Figures 5b and 5c, the mean MT solution is close to the true MT (represented by the magenta star) in the lune source-type diagram. The decomposition of the mean MT solution (Figure 6a) gives 65.5%ISO, 8.4%CLVD, and 26.2%DC, which agrees with 63.7% ISO, 6.4% CLVD, and 29.8% DC of the true MT. Its moment magnitude is M_w=5.22, which is close to the input M_w=5.21.

The evolution of MT solutions from low to high probability demonstrates the effectiveness of the employed search engine. The plot of the posterior probability in Figure 5c is consistent with the contour plot of variance reduction shown in Alvizuri & Tape (2018) by grid search over source types to achieve the best waveform fit. Moreover, based on the posterior probability, our method avoids most MTs in the ISO-CLVD tradeoff area and shows smaller MT uncertainty in the converging stage. The posterior distribution of each MT parameter is near Gaussian, as shown in Figure 5a, consistent with the assumption made when deriving the likelihood function in Section 2.2. The linear correlation between M_{xx}, M_{yy} and M_{zz} is a result of the tradeoff between pure ISO and vertical-CLVD components for shallow sources, as discussed in Section 2.5.

Apart from the MT parameters, the station-specific noise levels (Figure 7a) and time shifts (Figure 7b) are also recovered by the ensemble samplers. As mentioned before, all noise levels are fixed to a single value (1.0) in the current numerical experiment. The recovered mean noise levels for all stations are generally close to the input value. Besides, the recovered time shifts are also close to the input time shifts (Table 1). The posterior distributions of station-specific noise and time shift parameters show a Gaussian character. An excellent waveform fit (VR>99%) between the observed (black) and predicted waveforms (red) using the mean MT and time shifts is obtained in Figure 6b. Therefore, we conclude that the inversion framework using regional stations is successful.

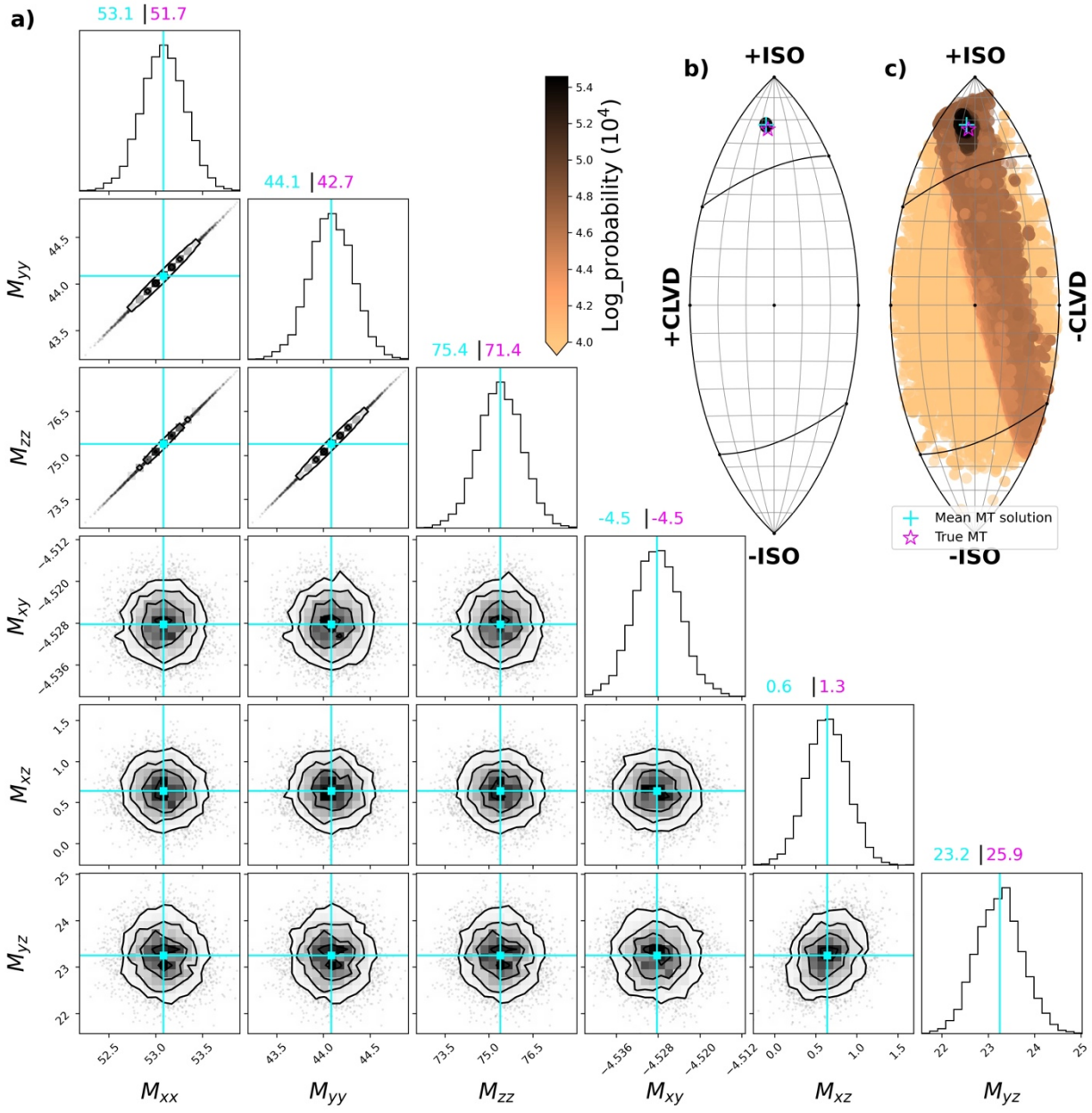

Figure 5. The synthetic scenario MT inversion considering uncorrelated data noise and 2D structural error within a hierarchical Bayesian inversion framework. The source depth is 0.5 km. Synthetic waveforms are filtered in the 20-50 s period band. (a) Each sub-panel shows a pair of the MT parameters in the convergency stage of the inversion. For a definition of the convergency stage, see the main text. The unit of MT parameters is 10^{15} Nm. The cyan lines are the MT parameters' means which are also indicated by the cyan numbers above each column, separated from the true (input) values (magenta numbers) by a vertical bar. (b)The lune diagram with the converging MT solution from (a). The magenta star shows the source type of the true MT input. The cyan cross shows the mean MT solution of the convergency stage. The color bar is used to display log probability. (c) The Lune source-type diagram shows the evolution of every 2 MT solutions during the entire inversion stage.

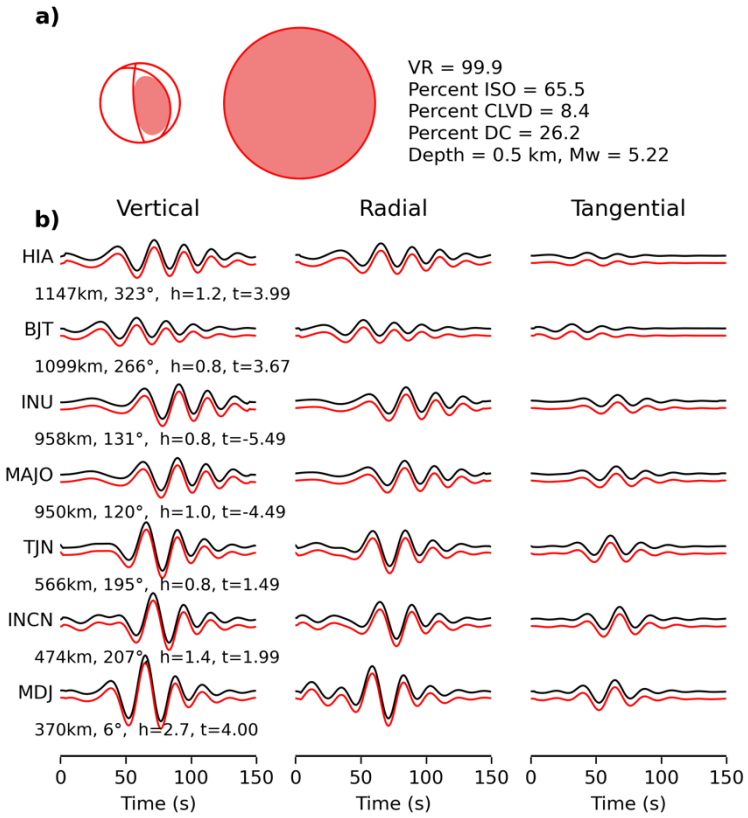

Figure 6. MT decomposition and waveform fit for the synthetic scenario. (a) Decomposition of MT solution into deviatoric (left) and isotropic (right) parts. The beachball sizes are proportional to the MT component percentages. (b) Waveform fit between 'observed' (black) and predicted (red) waveforms from the MT solution shown in (a), measured by the variance reduction. The waveforms are offset vertically for clarity. The numbers shown beneath the waveforms are source-receiver distance, azimuth, recovered station-specific noise parameter and time shift.

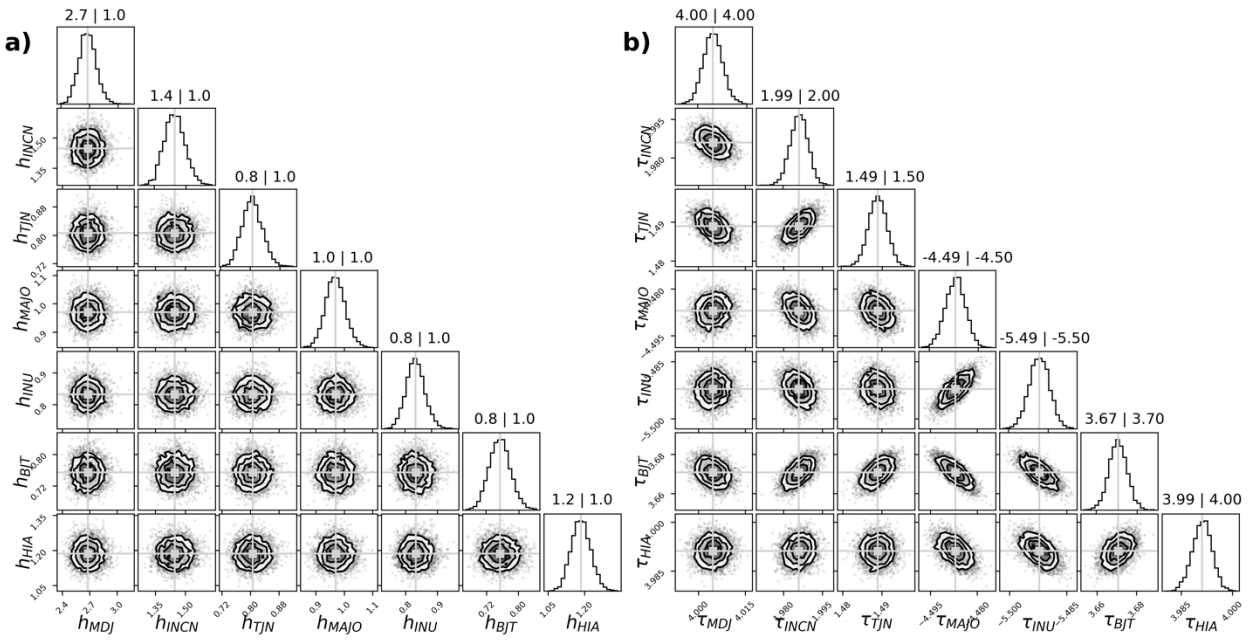

Figure 7. Recovered station-specific noise parameters (a) and time shifts (b) for the synthetic scenario. Each sub-panel shows a pair of parameters in the convergency stage of the inversion. The two numbers above each column are each parameter's mean and the true (input) values, respectively, which are separated by a vertical bar. The light gray lines show the mean values.

3.3 Sensitivity tests

Given that the inversion solution is sensitive to the presence and the way of treating the data noise, we consider its sensitivity against several scenarios, including different datasets corresponding to high, intermediate, and low SNR, different source depths, and different source types. The SNR is defined by

$$SNR = 20log_{10}(\frac{A_s}{C \cdot A_n}), \quad (13)$$

where A_s and A_n are the root mean square of the simulated waveform and 1-hour pre-event ambient noise amplitude. C is a component-based coefficient multiplying with the ambient noise to generate waveforms of specific SNR. We conducted six datasets of different SNRs from 5 to 30, with increments of five units. The real recorded data noise is correlated, and its correlated property should be considered in the noise model in an inversion problem; however, we argue that assuming uncorrelated noise is reasonable when the SNR is high.

The assumption of uncorrelated noise is reasonable in the cases of high SNR, while it may fail in the cases of low SNR. As shown in Figure 8a, the shallow source can be recovered in the case of high SNR ($SNR = 30$). The MT converges to a small area in orange, which is close to the true source (magenta star), with small uncertainty. As the correlated noise becomes more significant (i.e., SNR=25 or 20), the solution uncertainty also becomes more significant, and the theoretical tradeoff due to shallow depths becomes more challenging to mitigate. However, there is still a chance to retrieve the source parameters by only considering uncorrelated noise for intermediate-size earthquakes whose data SNR is usually above 20. For a typical SNR, i.e., 25,

this inversion method works for the same MT sources at depths varying from 0.5 to 3.0 km, as shown in Figure 8b. Besides, six different non-DC sources, including ISO-dominated and CLVD-dominated sources at the same depth of 0.5 km (Figure 8c), are also recovered with the uncorrelated noise model. However, in the case of low SNR data ($SNR = 10$ or 5), our algorithm, assuming uncorrelated noise, cannot reasonably recover the input MT. The solution uncertainty is substantial, as shown by the orange dots in the last two panels of Figure 8a, and the mean MT is far away from the true one. Besides, the theoretical tradeoff between ISO and CLVD remains unresolved due to the inappropriate noise estimate. This happens whenever noisy stations are involved or the earthquake is small.

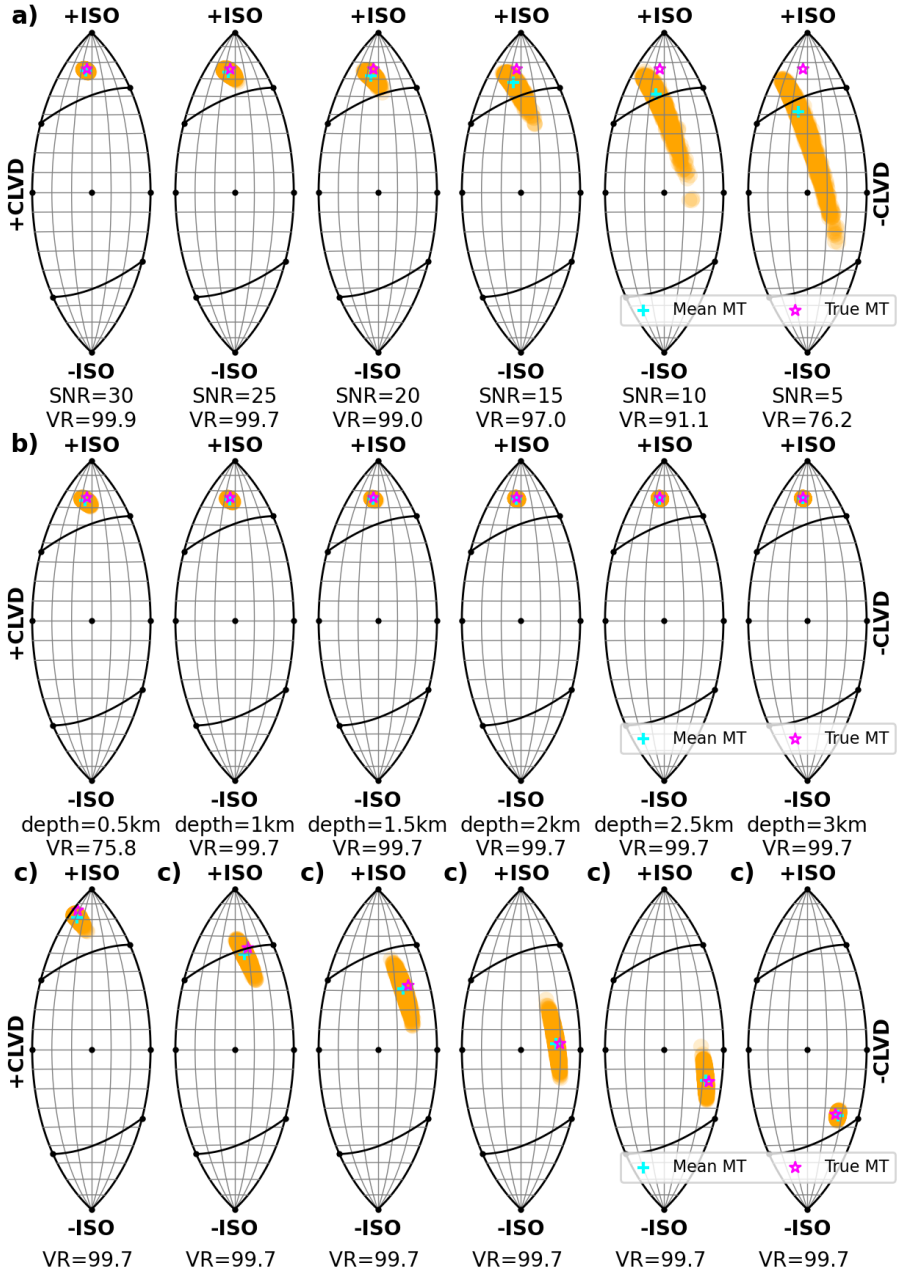

Figure 8. Source-type lune diagrams for recovered MT solutions in the following scenarios: (a) varying signal-to-noise ratios (SNR) from 30 to 5, with decrements by five units from left to rights, for the true source depth of 0.5 km; (b) varying true source depths from 0.5 to 3.0 km, with increments by 0.5 km, for the waveforms with SNR = 25; and (c) varying true source-types at the depth =0.5 km and SNR = 25. In each scenario, the source depth is treated as known. A magenta star represents the true MT in each panel. Overlapped orange dots are MT solutions in the convergency stage. A cyan cross marks their mean MT. The variance reduction between 'observed' and predicted waveforms from mean MT is shown beneath each panel. The noise in the simulated waveform is the pre-event noise multiplied by different factors to obtain "noisy waveforms" with given SNR.

4 Application for DPRK nuclear tests

4.1 Data preparation

Using lessons from the synthetic experiments, we now apply the developed MT inversion framework to the five DPRK nuclear tests between 2009 and 2017. The DPRK2006 test is not included in this study due to poor data quality. When possible, we use the same set of stations for all events to cross-check the recovered time shifts besides the recovered MT solutions. We choose five standard stations (i.e., MDJ, MAJO, INU, BJT, and HIA, as shown in Figure 1a) with sufficient SNR for each nuclear explosion. To fill the azimuth coverage gap in South Korea, the station INCN is added for the DPRK2009 test, the stations CHNB and YNCB for the DPRK2013 test, and the stations INCN and TJN for the three tests in 2016-2017. Finally, we used six stations for the DPRK2009 and seven for the DPRK2013-2017 tests. The recorded 3-component waveforms are corrected for the instrumental response to obtain displacements and filtered in the 20–50 second period band using a 4-corner acausal Butterworth bandpass filter. The waveforms are then incised into 150 s-windows starting at manually picked delay times after the origin times which are 50 s for stations MDJ, CHNB and YNCB, 70 s for INCN, 100 s for TJN, 200 s for MAJO and INU, and 280 s for BJT and HIA, respectively. The epicenter location and origin time used in this study are from Table 1 of Alvizuri and Tape (2018). GFs are calculated using the MDJ2 model (Ford et al., 2009) with a fixed depth of 0.5 km. The configuration of ensemble samplers is the same as used in synthetic experiments.

4.2 MT inversion results of DPRK2009-2017 tests

Figure 9 presents the entire evolution of the Monte-Carlo chains during the sampling for all five explosions. Like in the synthetic case, starting with randomly chosen MTs, our inversion method with ensemble samplers explores a wide variety of source types, including the ISO-CLVD tradeoff area (the darker stripe in each sub-panel) with a higher posterior probability. Finally, the chains converge to a small area with the highest posterior probability (consisting of black dots in each sub-panel in Figure 9). The evolution patterns of MTs are consistent among the five explosions, which, to some extent, agrees with the patterns obtained by grid search over source types to achieve the best waveform fit for the DPRK tests by Chiang et al. (2018) and Alvizuri & Tape (2018). Moreover, by accounting for the station-specific data noise and time shifts between predictions and observations (i.e., 2D structural error), our inversion method skips most MTs in the ISO-CLVD tradeoff area and shows smaller uncertainty of the MT solution in the convergency stage. The mean MT solution of each explosion, i.e., the cyan cross in each sub-panel, is calculated by averaging the MTs in this convergency stage. Figure 10 shows the excellent fit of the predicted waveforms corresponding to the mean MTs and the observed waveforms.

The source mechanisms recovered from the five DPRK explosions in 2009–2017 exhibit similar explosive nature. Large ISO components dominate their MT solutions, i.e., 43% in the DPRK2009 test and DPRK2013 test, and 50% in three DPRK2016-2017 tests, respectively, which indicates their explosive nature of sources. The three diagonal elements of mean MT solutions, M_{xx}, M_{yy}, and M_{zz}, are all positive and larger than off-diagonal elements, M_{xy}, M_{xz}, and M_{yz}. Furthermore, M_{xx} and M_{yy} are almost equal and smaller than M_{zz}, which indicates these five explosions are close to a crack source. The results also show significant CLVD components required in these five explosions (>=30%) and small DC components, e.g., 13% of

DC for the 2017 explosion. The high degree of similarity among these five explosions, i.e., near the ISO pole and close to the crack source in the source-type lune diagram, has already been pointed out by Liu et al. (2018) using a unique dataset that includes more broadband stations on the China side. Their similar long-period waveforms are responsible for this source similarity. However, the crack source mechanism for underground nuclear explosions remains unclear. Interestingly, our results coincide with the MTs of nuclear explosions at Nevada National Security Site obtained by Pasyanos & Chiang (2021) using MT inversion for 130 nuclear explosions from 1970 to 1996, which are also distributed around the crack source. Compared with other studies (e.g., Alvizuri & Tape, 2018; Chiang et al., 2018), we report slightly higher moment magnitudes, i.e., $\mathrm{M_w} = 4.69$, $\mathrm{M_w} = 4.93$, $\mathrm{M_w} = 5.0$, $\mathrm{M_w} = 5.13$, and $\mathrm{M_w} = 5.79$, respectively. The values obtained are closer to the moment magnitudes that Liu et al. (2018) obtained.

The station-specific uncorrelated noise levels and time shifts are recovered as free parameters in the inversion. The noise parameter is relative to the standard deviation calculated from 1-hour pre-event ambient noise records. As shown in Figure 10, the noise parameter of MDJ is the smallest for all explosions. At the same time, MAJO and INU stations have the most significant noise parameters. This result agrees with the perfect waveform fit at MDJ and the poorer waveform fit at MAJO and INU stations. Note that the contribution of each station is quantified by the likelihood function instead of only data noise strength because the data noise C_i in Equation 9 has two competing effects on the likelihood function (Bodin et al., 2012). The resulting likelihood reflects the importance of each station (Shang & Tkalčić, 2020).

A visual comparison of individual station contributions reveals their relative significance in the overall solution. For example, Figure 11 shows the logarithm of the likelihood (log-likelihood) for all stations used in the inversion for DPRK2017 (plots for the other four explosions can be found in Figure S1), and the station MDJ plays the most critical role because it presents the highest likelihood. The MDJ is the closest station to the sources and has a high SNR. Overall, MDJ, INCN, and BJT are the most important stations that drive the DPRK2017 MT inversion, while stations MAJO and INU on the Japanese side only have least contributions.

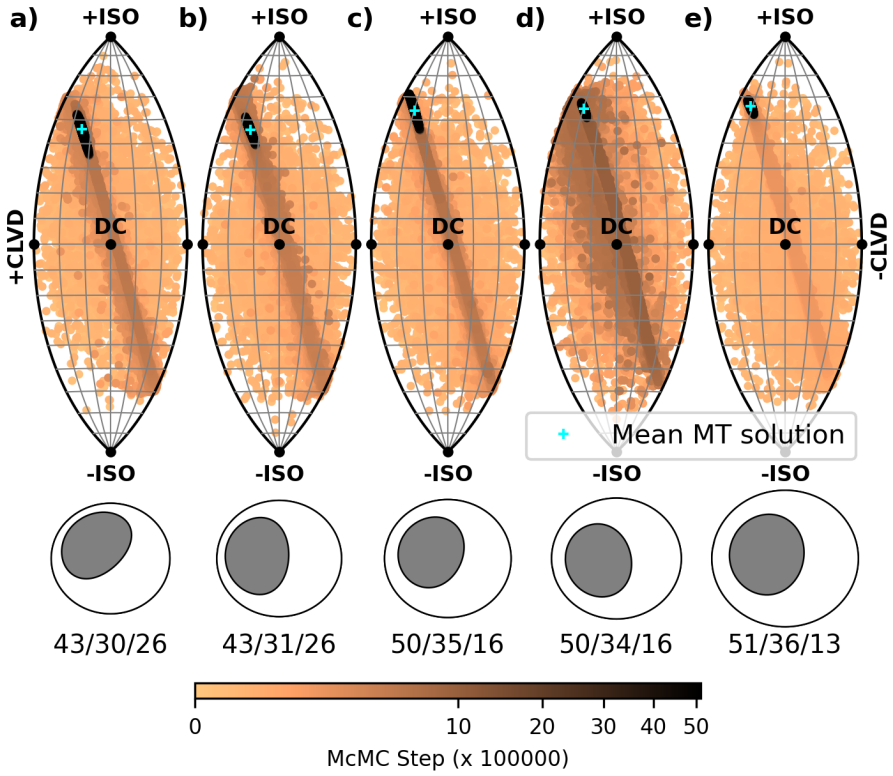

Figure 9. Source type lune diagrams for the five DPRK tests shown chronologically from 2009 to 2017: (a) DPRK2009, (b) DPRK2013, (c) DPRK2016a (6 Jan 2016), (d) DPRK2016b (9 Sep 2016), and (e) DPRK2017. The color bar indicates the equivalent inversion steps with the power law normalization of 2/5 for clearer viewing of the convergence. In each panel, the overlapping color-coded dots show the MT evolution as the inversion step increases. The cyan cross is the mean MT of the convergency stage for each explosion. The resulting mechanisms are shown by the beachballs. The size of each beachball is proportional to its moment magnitude. The numbers below each beachball are a percentage of ISO, CLVD, and DC, respectively.

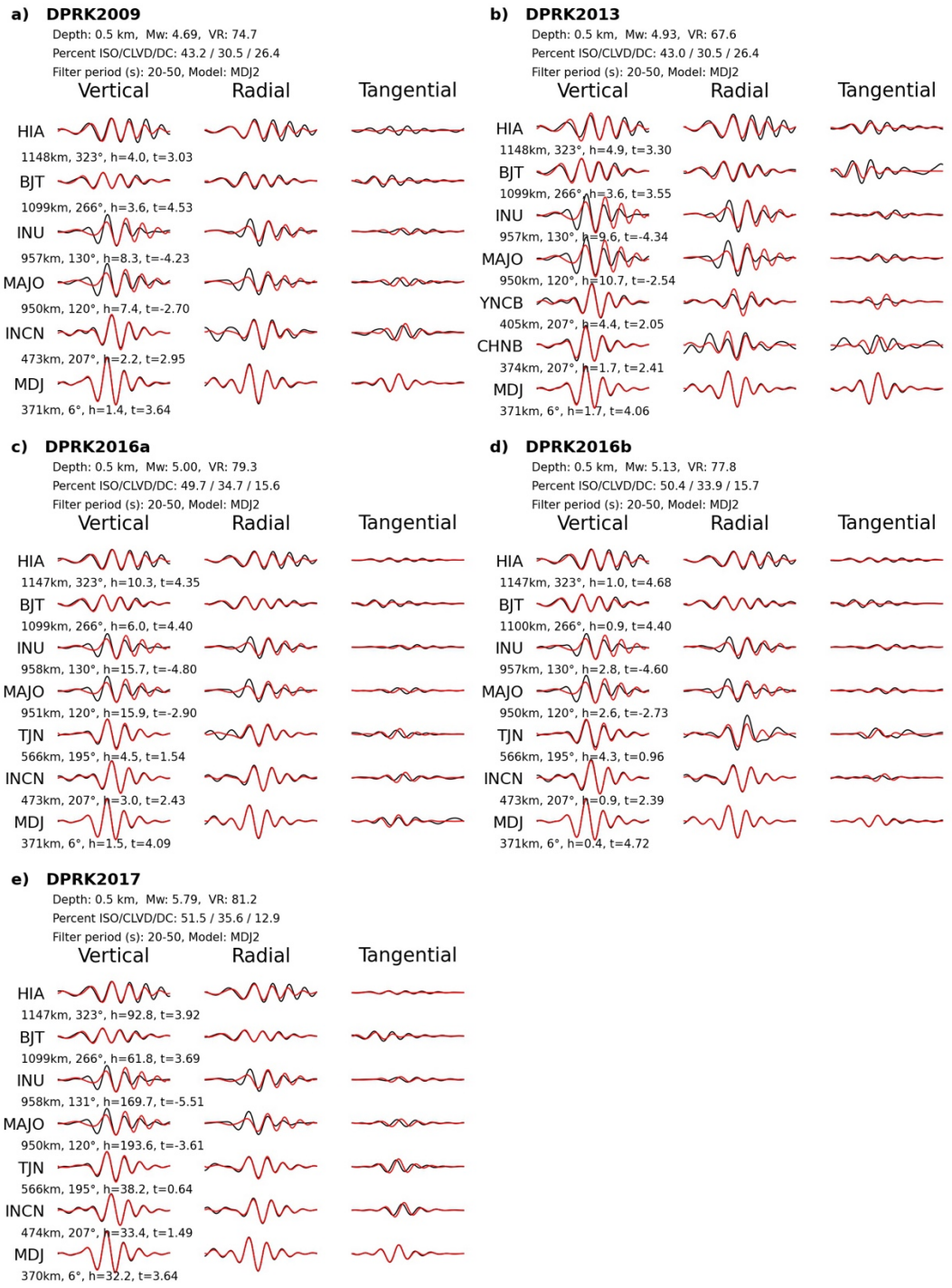

Figure 10. Fits between observed (black) and predicted (red) waveforms for the five DPRK explosions shown chronologically: (a) DPRK2009, (b) DPRK2013, (c) DPRK2016a (6 Jan 2016), (d) DPRK2016b (9 Sep 2016), and (e) DPRK2017. The same 4-corner acausal bandpass (20–50 s) filter was used for each explosion. The numbers shown beneath each station are the source-station distance, azimuth, the recovered station-specific noise parameter and time shift in seconds.

608

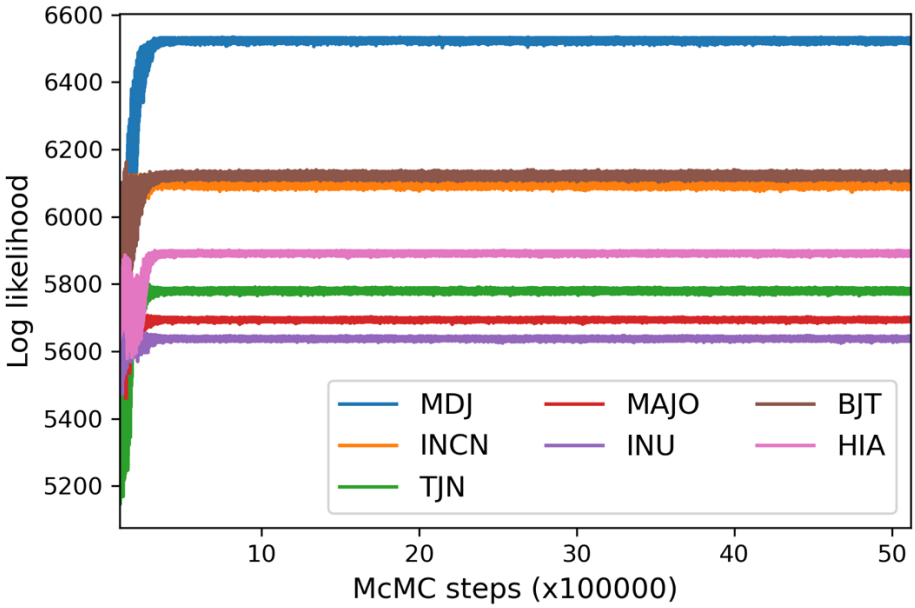

609

610 **Figure 11.** Log-likelihood for each station in the DRPK2017 MT inversion. Most burn-in steps
611 are discarded to illustrate the likelihood function in the convergency stage.

612 The recovered station-specific time shifts from five explosions reveal a consistent pattern,
613 which demonstrates the robustness of our Bayesian MT inversion. Table 2 lists the station-
614 specific time shifts from five explosions obtained in this study. Firstly, time shifts at the same
615 stations are similar among the five explosions: three stations in China (MDJ, BJT, and HIA)
616 have positive time shifts (up to 4.72 s), stations in South Korea (INCN, TJN, CHNB, and
617 YNCB) have smaller positive time shifts (0.64 – 2.95 s), while two stations in Japan require
618 negative time shifts (up to -5.51 s). The time shifts at the same station remain of the same sign
619 even though the actual values vary in different inversions. This is because the possible errors in
620 event origin times also contribute to the time shifts in the observed data. From the waveform fit
621 in Figure 10, some small residual time shifts remain on the tangential components, likely due to
622 ignoring the structures' anisotropy by applying the same time shift for all three components at
623 each station. Treating the anisotropy using two-time shifts per station, one for vertical/radial
624 components sensitive to vertically polarized Rayleigh waves and the other for horizontally
625 polarized Love waves, is the subject of future studies. To summarize the results, we average the
626 time shifts on each station for various inversions and plot their distribution with respect to the
627 MDJ2 velocity model in Figure 12.

628 The distribution of station-specific time shifts coincides with the regional 2D structures
629 surrounding the test site. In this study, the station-specific time shift between observations and
630 predictions accounts for the possible deviation of Earth structure along specific paths with
631 respect to the assumed 1D Earth model (i.e., MDJ2 model) for the entire study region. Positive
632 time shifts indicate that the MDJ2 model is faster than the actual Earth's structure along these
633 paths, while negative time shifts suggest that the MDJ2 model is slower than the actual Earth's
634 structure. As seen in Figure 12, the Korean Peninsula is at the margin of continental crust to the
635 west and north and oceanic crust to the east in the Japanese Sea. Therefore, the paths of surface

636 waves to stations in Japan (i.e., MAJO and INU) are sensitive primarily to the high-speed
637 mantle, which protrudes to shallower depths beneath a thin oceanic crust. Two stations in Japan
638 hence require negative time shifts because the MDJ2 model is slower. The paths of surface
639 waves to stations in China (MDJ, BJT, and HHIA) are sensitive to a relatively slower, thick
640 continental crust. Three stations in China require positive time shifts because the MDJ2 model is
641 faster. Furthermore, the two stations in South Korea require smaller positive time shifts
642 compared with the three stations in China. That could be due to the variation of continental crust
643 thickness along the paths. Thus, overall, the recovered time shifts are consistent with the regional
644 geological structures of the study region.

645 **Table 2**. Recovered station-specific time shifts (Unit: second) for five DPRK2009-2017 tests. For
646 the DPRK2013 test, the two stations in South Korea were CHNB and YNCB.

Explosions	**IC.MDJ**	**IC.BJT**	**IC.HIA**	**IU.INCN**	**KG.TJN**	**IU.MAJO**	**G.INU**
DPRK2009	3.64	4.53	3.03	2.95		-2.7	-4.23
DPRK2013	4.06	3.55	3.3	2.41(CHNB)	2.05(YNCB)	-2.54	-4.34
DPRK2016a	4.09	4.4	4.35	2.43	1.54	-2.9	-4.8
DPRK2016b	4.72	4.4	4.68	2.39	0.96	-2.73	-4.6
DPRK2017	3.64	3.69	3.92	1.49	0.64	-3.61	-5.51

647

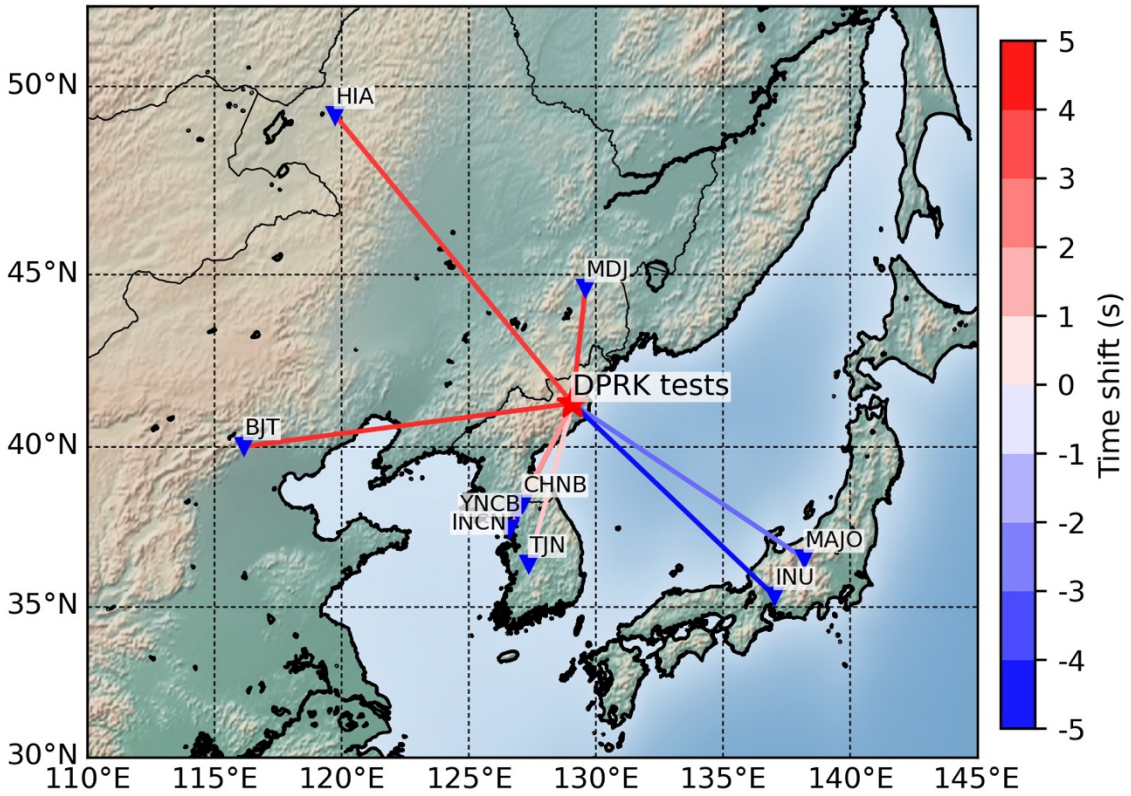

Figure 12. The mean time shift at each station. Positive time shifts (red) result from shifting the predicted waveforms forward, while negative time shifts (blue) stem from shifting the predicted waveforms backward.

4.3 Robustness of the MT inversion

Here we discuss the robustness of the proposed Bayesian MT inversion in three aspects. Firstly, these five DPRK explosions can arguably be considered five repetitive, shallow sources with different moment magnitudes. We used the same data preprocessing, similar source-station configuration, and the same 1D Earth model to perform the seismic source inversions. Our Bayesian MT inversion provides similar results for these five explosions, including MT solutions and station-specific time shifts.

Secondly, as noted above, the two stations in Japan, i.e., MAJO and INU, play a less important role than the other five stations in the source inversion for the DPRK2017 event. Therefore, we are motivated to remove these two stations and only use the other five stations in South Korea and China to invert the DPRK2017 event's MT. The solution is shown in Figure S2 and is close to a crack source mechanism, with 52% ISO, 37% CLVD, 11% DC, and a moment magnitude of 5.8. It is consistent with the source obtained from seven stations in Figure 9e. The recovered station-specific time shifts and noise parameters (Figure S2c) also remain stable compared with those of the seven stations shown in Figure 10e. The variance reduction of waveform fit improves from 81.2% to 92.2% because two stations with a poorer fit are neglected in the inversion.

Thirdly, to demonstrate our approach's robustness, we use another unique dataset from seven other stations closer to the Punggye-ri test site (Figure S3a) to invert the DPRK2017 event's MT. We apply the same band-pass filter to the waveforms and manually pick 150s-window waveforms. The inversion result using the same velocity model (i.e., MDJ2) shows a similar character to the previous dataset in Figure 9e. The source is dominated by an ISO=54% and is close to the crack source type. The CLVD component is up to 38%, and the DC component is negligible (only 8%), with a smaller contribution than the result shown in Figure 9e. The pattern of recovered station-specific time shifts (Figure S3a) agrees with Table 2. Four stations (KSA, CHNB, CHC2, and OKEB) where the surface waves propagated through a combination of thin oceanic and thick continental crust require a slight positive time shift. Three stations (NSN, MDJ, and DACB) need more significant time shifts because the surface waves mainly propagate through the thick continental crust. In addition, these two datasets include a common station, MDJ. The time shift and noise parameter at this station from two inversions remain stable, specifically, ~3.6 s time shift and ~32 for noise parameter. Therefore, we conclude that our new hierarchical Bayesian MT inversion algorithm is robust under the same assumption of Earth's structure.

5 Discussion

5.1 The effect of the uncorrelated noise assumption

In this study, we assume the uncorrelated data noise using a diagonal covariance matrix C_i and focus on another, arguably more critical uncertainty (2D structural error). As demonstrated in the synthetic experiments (Section 3.3), this assumption of uncorrelated noise succeeds in the cases of high SNR (25 or larger) while failing in the cases of low SNR. From Figure 9, the MT solutions of the DPRK2009, DPRK2013, and DPRK2016a events show more considerable uncertainty than those of the DPRK2016b and DPRK2017 events. Possibly, a more comprehensive treatment of data noise should be conducted for these three explosions. For instance, Mustać et al. (2020) accounted for correlated noise with empirical noise covariance matrices, obtaining a large ISO composition (about 70%) for the DPRK2013 event at the preferable source depth of 2 km. Here, taking advantage of the affine-invariant ensemble samplers, we fix the sources at a near-surface depth, i.e., 0.5 km. This is the highlight of the present study because setting the depth near the surface in the presence of the ISO-CLVD tradeoffs was a challenging aspect in previous DPRK explosion studies.

We note that the uncorrelated data noise is still a significant aspect of the source inversion. To illustrate its significance, we fix the noise level at each station to 1.0 instead of inverting it. This means the noise strength is assumed to be the same as pre-event ambient noise. The MT inversions for the five explosions are plotted in Figure S4. Relaxing the noise levels as free parameters increased the ISO components by ~21% for the DPRK2009 event, ~15% for the DPRK2013 event, ~22% for the DPRK2016a event, and ~6% for the DPRK2016b and DPRK2017 events. Besides, the recovered noises at different stations do not appear to have a specific pattern for the five considered explosions. This is explainable given that the ambient noise at each station could be primarily influenced by instantaneous conditions at recording sites, e.g., the seasonal variations. These five explosions happened at different times with significant time gaps.

5.2 Uncertainty of MT for shallow explosions

Previous MT inversions of the DPRK events confirmed the explosive source nature by recovering a significant ISO component (Alvizuri & Tape, 2018; Chiang et al., 2018; Dreger et al., 2021; Liu et al., 2018; Mustać et al., 2020; Wang et al., 2018; Xu et al., 2020). However, as we discussed, an MT inversion can suffer severe uncertainty due to several issues. Firstly, there is an ambiguity between ISO and vertical CLVD mechanisms for very shallow source depths. This is because the long-period waveforms at regional stations are most sensitive to the radiated energy along the equator of the focal sphere with large take-off angles, where the pure ISO and vertical CLVD emit similar surface waves at regional distances. Their significant difference in radiation pattern happens only for small take-off angles, meaning teleseismic data are required to distinguish them, as suggested by Ford et al. (2012) and Chiang et al. (2014).

Secondly, the region surrounding the Punggye-ri test site comprises a complex structural setting (e.g., Mustać et al., 2020), located at a margin of the continental crust in the west to the oceanic crust in the east across the Sea of Japan (East Sea). Using a 1D velocity model ignoring this strong 3D structure effect may result in uncertainty to MT inversion. This study uses the station-based time shift between synthetics and observations to treat this significant 3D structural effect on specific source-station paths.

Thirdly, data noise can also introduce uncertainty to MT solutions. These effects are barely considered for the DPRK explosions in previous studies. As shown in Figure 13, five previous studies and this study of the DPRK2017 event gave different MTs even though all of them obtained a high ISO content and fit the observed waveforms with high VR, spanning from 75% to 95%. The differences testify to and confirm the inversion's non-uniqueness. This study's moment magnitude and MTs results are most similar to those of Liu et al. (2018), using a different 1D velocity model and an independent dataset in the 0.03-0.09 Hz band.

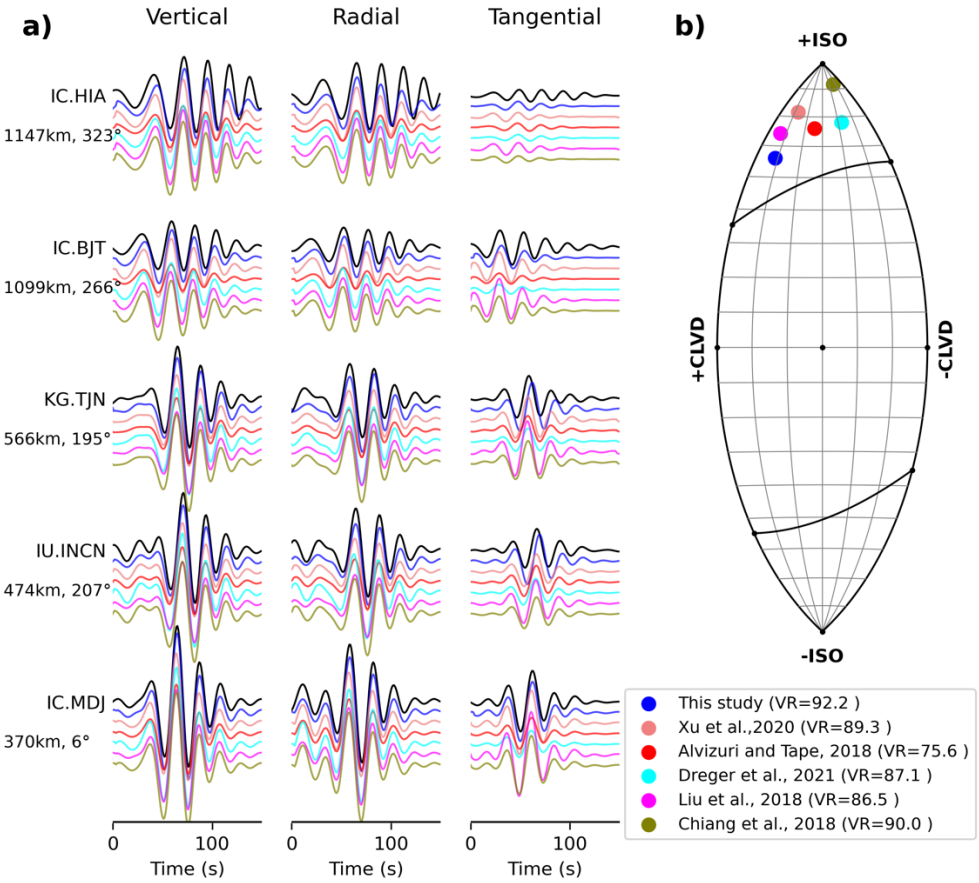

Figure 13. The fits between observed (black) and predicted waveforms (color-coded lines) obtained from five previous studies (see the legend) and this study for the DPRK2017 test. The predicted waveforms in this study are shifted using the recovered time shifts. In contrast, the other five sets of predicted waveforms are shifted using the times that give the highest cross-correlation coefficient to the observations. The fit levels (i.e., variance reduction) are listed in panel (b) legend.

6 Conclusions

In this study, we consider the uncertainty due to data noise involved in the data acquisition process and structural uncertainty along specific source-station paths due to imperfect knowledge of Earth structure (i.e., 2D structural error) for full MT inversion within the hierarchical Bayesian framework. The data noise on each component is assumed to be uncorrelated and measured by a standard deviation determined by an inversion in a manner of a free parameter. Besides, we use the station-specific time shifts between observed and predicted waveforms to address the 2D structural uncertainty. Unlike previous studies, the time shifts are relaxed as free parameters, determined simultaneously with noise and moment tensor parameters. We demonstrate the feasibility of this method via well-designed synthetic experiments.

Then we perform MT inversions for the five DPRK nuclear explosions from 2009 to 2017. The MT inversion results indicate that the five explosions feature high degrees of similarity. A significant ISO component dominates their sources, i.e., 43% for the DPRK2009

and DPRK2013 events, and 50% for the DPRK2016a, DPRK2016b, and DPRK2017 events, respectively, which confirms the nature of the explosive source. Additionally, the five events have significant CLVD components (30%, 31%, 35%, 34%, and 36%). The DC components are small: 26%, 26%, 16%, 16%, and 13%, respectively. Relaxing the station-based data noise strength also plays a vital role in the MT inversion for DPRK explosions by increasing the ISO components. The likelihood function combining the noise and waveform residuals weights stations' contribution differently. Moreover, the recovered station-based time shifts recover the 2D Earth structure character in the surrounding region of these nuclear events, demonstrating that our method appropriately accounts for the 2D structural heterogeneities.

Rigorously treating structural errors, especially incorporating the effects of 3D structural heterogeneity, is at leading-edge research in seismic source inversion. This study can be considered a transitional solution between incorporating the 1D to 3D Earth models in the regional MT inversion.

Data Availability Statement

Seismic waveform data at seven stations, MDJ, HIA, BJT, MAJO, INU, INCN and TJN used in this study are freely downloaded from Incorporated Research Institution for Seismology Data Management Center (IRIS DMC, http://ds.iris.edu/ds/nodes/dmc/) using ObsPy software package (Beyreuther et al., 2010). Seismic waveform data at other stations (e.g., CHNB and YNCB) come from local networks operated by the Korea Institute of Geoscience and Mineral Resources (KIGAM) and the Korea Meteorological Administration (KMA).

Acknowledgments

This work was supported by DoD AFRL Grant contract number: FA9453-20-C-0072. All the figures are made with Matplotlib (Hunter, 2007).

References

Aki, K., & Richards, P. G. (2002). *Quantitative seismology* (2. ed., corr. print). Mill Valley, Calif: Univ. Science Books.

Alvizuri, C., & Tape, C. (2018). Full Moment Tensor Analysis of Nuclear Explosions in North Korea. *Seismological Research Letters*, *89*(6), 2139–2151. https://doi.org/10.1785/0220180158

Alvizuri, C., Silwal, V., Krischer, L., & Tape, C. (2018). Estimation of Full Moment Tensors, Including Uncertainties, for Nuclear Explosions, Volcanic Events, and Earthquakes. *Journal of Geophysical Research: Solid Earth*, *123*(6), 5099–5119. https://doi.org/10.1029/2017JB015325

Bayes, Mr., & Price, Mr. (1763). An Essay towards Solving a Problem in the Doctrine of Chances. By the Late Rev. Mr. Bayes, F. R. S. Communicated by Mr. Price, in a Letter to John Canton, A. M. F. R. S. *Philosophical Transactions (1683-1775)*, *53*, 370–418.

Beyreuther, M., Barsch, R., Krischer, L., Megies, T., Behr, Y., & Wassermann, J. (2010). ObsPy: A Python Toolbox for Seismology. *Seismological Research Letters*, *81*(3), 530–533. https://doi.org/10.1785/gssrl.81.3.530

795 Bodin, T., Sambridge, M., Gallagher, K., & Rawlinson, N. (2012). Transdimensional inversion
796 of receiver functions and surface wave dispersion. *Journal of Geophysical Research:*
797 *Solid Earth*, *117*(B2). https://doi.org/10.1029/2011JB008560

798 Cesca, S., Buforn, E., & Dahm, T. (2006). Amplitude spectra moment tensor inversion of
799 shallow earthquakes in Spain. *Geophysical Journal International*, *166*(2), 839–854.
800 https://doi.org/10.1111/j.1365-246X.2006.03073.x

801 Cesca, Simone, Heimann, S., Stammler, K., & Dahm, T. (2010). Automated procedure for point
802 and kinematic source inversion at regional distances. *Journal of Geophysical Research:*
803 *Solid Earth*, *115*(B6). https://doi.org/10.1029/2009JB006450

804 Chiang, A., Dreger, D. S., Ford, S. R., & Walter, W. R. (2014). Source Characterization of
805 Underground Explosions from Combined Regional Moment Tensor and First-Motion
806 Analysis. *Bulletin of the Seismological Society of America*, *104*(4), 1587–1600.
807 https://doi.org/10.1785/0120130228

808 Chiang, A., Ichinose, G. A., Dreger, D. S., Ford, S. R., Matzel, E. M., Myers, S. C., & Walter,
809 W. R. (2018). Moment Tensor Source-Type Analysis for the Democratic People's
810 Republic of Korea–Declared Nuclear Explosions (2006–2017) and 3 September 2017
811 Collapse Event. *Seismological Research Letters*, *89*(6), 2152–2165.
812 https://doi.org/10.1785/0220180130

813 Dahm, T., Manthei, G., & Eisenblätter, J. (1999). Automated moment tensor inversion to
814 estimate source mechanisms of hydraulically induced micro-seismicity in salt rock.
815 *Tectonophysics*, *306*(1), 1–17. https://doi.org/10.1016/S0040-1951(99)00041-4

816 Dettmer, J., Dosso, S. E., & Holland, C. W. (2007). Uncertainty estimation in seismo-acoustic
817 reflection travel time inversion. *The Journal of the Acoustical Society of America*, *122*(1),
818 161–176. https://doi.org/10.1121/1.2736514

819 Dillinger, W. H., Harding, S. T., & Pope, A. J. (1972). Determining Maximum Likelihood Body
820 Wave Focal Plane Solutions. *Geophysical Journal International*, *30*(3), 315–329.
821 https://doi.org/10.1111/j.1365-246X.1972.tb05817.x

822 Donner, S., Mustać, M., Hejrani, B., Tkalčić, H., & Igel, H. (2020). Seismic moment tensors
823 from synthetic rotational and translational ground motion: Green's functions in 1-D
824 versus 3-D. *Geophysical Journal International*, *223*(1), 161–179.
825 https://doi.org/10.1093/gji/ggaa305

826 Dreger, D. S., Tkalčić, H., & Johnston, M. (2000). Dilational Processes Accompanying
827 Earthquakes in the Long Valley Caldera. *Science*, *288*(5463), 122–125.
828 https://doi.org/10.1126/science.288.5463.122

829 Dreger, D. S., Gritto, R., & Nelson, O. (2021). Path Calibration of the Democratic People's
830 Republic of Korea 3 September 2017 Nuclear Test. *Seismological Research Letters*.
831 https://doi.org/10.1785/0220210105

832 Duputel, Z., & Rivera, L. (2019). The 2007 caldera collapse of Piton de la Fournaise volcano:
833 Source process from very-long-period seismic signals. *Earth and Planetary Science*
834 *Letters*, *527*, 115786. https://doi.org/10.1016/j.epsl.2019.115786

Duputel, Z., Rivera, L., Fukahata, Y., & Kanamori, H. (2012). Uncertainty estimations for seismic source inversions: Uncertainty estimations for source inversions. *Geophysical Journal International*, *190*(2), 1243–1256. https://doi.org/10.1111/j.1365-246X.2012.05554.x

Duputel, Z., Agram, P. S., Simons, M., Minson, S. E., & Beck, J. L. (2014). Accounting for prediction uncertainty when inferring subsurface fault slip. *Geophysical Journal International*, *197*(1), 464–482. https://doi.org/10.1093/gji/ggt517

Dziewonski, A. M., Chou, T.-A., & Woodhouse, J. H. (1981). Determination of earthquake source parameters from waveform data for studies of global and regional seismicity. *Journal of Geophysical Research: Solid Earth*, *86*(B4), 2825–2852. https://doi.org/10.1029/JB086iB04p02825

Eaton, D. W., & Mahani, A. B. (2015). Focal Mechanisms of Some Inferred Induced Earthquakes in Alberta, Canada. *Seismological Research Letters*, *86*(4), 1078–1085. https://doi.org/10.1785/0220150066

Ebel, J. E., & Bonjer, K.-P. (1990). Moment tensor inversion of small earthquakes in southwestern Germany for the fault plane solution. *Geophysical Journal International*, *101*(1), 133–146. https://doi.org/10.1111/j.1365-246X.1990.tb00763.x

Ekström, G., Nettles, M., & Dziewoński, A. M. (2012). The global CMT project 2004–2010: Centroid-moment tensors for 13,017 earthquakes. *Physics of the Earth and Planetary Interiors*, *200–201*, 1–9. https://doi.org/10.1016/j.pepi.2012.04.002

Fichtner, A., & Tkalčić, H. (2010). Insights into the kinematics of a volcanic caldera drop: Probabilistic finite-source inversion of the 1996 Bárdarbunga, Iceland, earthquake. *Earth and Planetary Science Letters*, *297*(3–4), 607–615. https://doi.org/10.1016/j.epsl.2010.07.013

Ford, S. R., Dreger, D. S., & Walter, W. R. (2009). Source analysis of the Memorial Day explosion, Kimchaek, North Korea. *Geophysical Research Letters*, *36*(21). https://doi.org/10.1029/2009GL040003

Ford, S. R., Walter, W. R., & Dreger, D. S. (2012). Event Discrimination using Regional Moment Tensors with Teleseismic-P Constraints. *Bulletin of the Seismological Society of America*, *102*(2), 867–872. https://doi.org/10.1785/0120110227

Foreman-Mackey, D., Hogg, D. W., Lang, D., & Goodman, J. (2013). emcee: The MCMC Hammer. *Publications of the Astronomical Society of the Pacific*, *125*(925), 306–312. https://doi.org/10.1086/670067

Gallovič, F., Käser, M., Burjánek, J., & Papaioannou, C. (2010). Three-dimensional modeling of near-fault ground motions with nonplanar rupture models and topography: Case of the 2004 Parkfield earthquake. *Journal of Geophysical Research: Solid Earth*, *115*(B3). https://doi.org/10.1029/2008JB006171

Gilbert, F. (1971). Excitation of the Normal Modes of the Earth by Earthquake Sources. *Geophysical Journal International*, *22*(2), 223–226. https://doi.org/10.1111/j.1365-246X.1971.tb03593.x

875 Goodman, J., & Weare, J. (2010). Ensemble samplers with affine invariance. *Communications in*
876 *Applied Mathematics and Computational Science*, *5*(1), 65–80.
877 https://doi.org/10.2140/camcos.2010.5.65

878 Gouveia, W. P., & Scales, J. A. (1998). Bayesian seismic waveform inversion: Parameter
879 estimation and uncertainty analysis. *Journal of Geophysical Research: Solid Earth*,
880 *103*(B2), 2759–2779. https://doi.org/10.1029/97JB02933

881 Hallo, M., & Gallovič, F. (2016). Fast and cheap approximation of Green function uncertainty
882 for waveform-based earthquake source inversions. *Geophysical Journal International*,
883 *207*(2), 1012–1029. https://doi.org/10.1093/gji/ggw320

884 Hardebeck, J. L. (2002). A New Method for Determining First-Motion Focal Mechanisms.
885 *Bulletin of the Seismological Society of America*, *92*(6), 2264–2276.
886 https://doi.org/10.1785/0120010200

887 Hastings, W. K. (1970). Monte Carlo sampling methods using Markov chains and their
888 applications. *Biometrika*, *57*(1), 97–109. https://doi.org/10.1093/biomet/57.1.97

889 Hejrani, B., & Tkalčić, H. (2020). Resolvability of the Centroid-Moment-Tensors for Shallow
890 Seismic Sources and Improvements From Modeling High-Frequency Waveforms.
891 *Journal of Geophysical Research: Solid Earth*, *125*(7).
892 https://doi.org/10.1029/2020JB019643

893 Hejrani, B., Tkalčić, H., & Fichtner, A. (2017). Centroid moment tensor catalogue using a 3-D
894 continental scale Earth model: Application to earthquakes in Papua New Guinea and the
895 Solomon Islands. *Journal of Geophysical Research: Solid Earth*, *122*(7), 5517–5543.
896 https://doi.org/10.1002/2017JB014230

897 Hingee, M., Tkalčić, H., Fichtner, A., & Sambridge, M. (2011). Seismic moment tensor
898 inversion using a 3-D structural model: applications for the Australian region.
899 *Geophysical Journal International*, *184*(2), 949–964. https://doi.org/10.1111/j.1365-
900 246X.2010.04897.x

901 Hunter, J. D. (2007). Matplotlib: A 2D Graphics Environment. *Computing in Science &*
902 *Engineering*, *9*(3), 90–95. https://doi.org/10.1109/MCSE.2007.55

903 Johnson, L. R. (2014). Source Mechanisms of Induced Earthquakes at The Geysers Geothermal
904 Reservoir. *Pure and Applied Geophysics*, *171*(8), 1641–1668.
905 https://doi.org/10.1007/s00024-014-0795-x

906 Jost, M. L., & Herrmann, R. B. (1989). A Student's Guide to and Review of Moment Tensors.
907 *Seismological Research Letters*, *60*(2), 37–57. https://doi.org/10.1785/gssrl.60.2.37

908 Julian, B. R. (1986). Analysing seismic-source mechanisms by linear-programming methods.
909 *Geophysical Journal International*, *84*(2), 431–443. https://doi.org/10.1111/j.1365-
910 246X.1986.tb04364.x

911 Julian, Bruce R. (1983). Evidence for dyke intrusion earthquake mechanisms near Long Valley
912 caldera, California. *Nature*, *303*(5915), 323–325. https://doi.org/10.1038/303323a0

913 Julian, Bruce R., & Foulger, G. R. (1996). Earthquake mechanisms from linear-programming
914 inversion of seismic-wave amplitude ratios. *Bulletin of the Seismological Society of*
915 *America*, *86*(4), 972–980. https://doi.org/10.1785/BSSA0860040972

916 Julian, Bruce R., Miller, A. D., & Foulger, G. R. (1998). Non-double-couple earthquakes 1.
917 Theory. *Reviews of Geophysics*, *36*(4), 525–549. https://doi.org/10.1029/98RG00716

918 Kanamori, H., & Given, J. W. (1982). Analysis of long-period seismic waves excited by the May
919 18, 1980, eruption of Mount St. Helens—A terrestrial monopole? *Journal of Geophysical*
920 *Research: Solid Earth*, *87*(B7), 5422–5432. https://doi.org/10.1029/JB087iB07p05422

921 Kawakatsu, H. (1996). Observability of the isotropic component of a moment tensor.
922 *Geophysical Journal International*, *126*(2), 525–544. https://doi.org/10.1111/j.1365-
923 246X.1996.tb05308.x

924 Kim, Y., Liu, Q., & Tromp, J. (2011). Adjoint centroid-moment tensor inversions. *Geophysical*
925 *Journal International*, *186*(1), 264–278. https://doi.org/10.1111/j.1365-
926 246X.2011.05027.x

927 Knopoff, L., & Randall, M. J. (1970). The compensated linear-vector dipole: A possible
928 mechanism for deep earthquakes. *Journal of Geophysical Research (1896-1977)*, *75*(26),
929 4957–4963. https://doi.org/10.1029/JB075i026p04957

930 Konstantinou, K. I., Kao, H., Lin, C.-H., & Liang, W.-T. (2003). Analysis of broad-band
931 regional waveforms of the 1996 September 29 earthquake at Bárdarbunga volcano,
932 central Iceland: investigation of the magma injection hypothesis, 12.

933 Liu, J., Li, L., Zahradník, J., Sokos, E., & Plicka, V. (2018). Generalized Source Model of the
934 North Korea Tests 2009–2017. *Seismological Research Letters*, *89*(6), 2166–2173.
935 https://doi.org/10.1785/0220180106

936 Martínez-Garzón, P., Kwiatek, G., Bohnhoff, M., & Dresen, G. (2017). Volumetric components
937 in the earthquake source related to fluid injection and stress state. *Geophysical Research*
938 *Letters*, *44*(2), 800–809. https://doi.org/10.1002/2016GL071963

939 Metropolis, N., Rosenbluth, A. W., Rosenbluth, M. N., Teller, A. H., & Teller, E. (1953).
940 Equation of state calculations by fast computing machines.
941 https://doi.org/10.1063/1.1699114

942 Miller, A. D., Foulger, G. R., & Julian, B. R. (1998). Non-double-couple earthquakes 2.
943 Observations. *Reviews of Geophysics*, *36*(4), 551–568.
944 https://doi.org/10.1029/98RG00717

945 Minson, S. E., & Dreger, D. S. (2008). Stable inversions for complete moment tensors.
946 *Geophysical Journal International*, *174*(2), 585–592. https://doi.org/10.1111/j.1365-
947 246X.2008.03797.x

948 Mustać, M., & Tkalčić, H. (2016). Point source moment tensor inversion through a Bayesian
949 hierarchical model. *Geophysical Journal International*, *204*(1), 311–323.
950 https://doi.org/10.1093/gji/ggv458

951 Mustać, M., & Tkalčić, H. (2017). On the Use of Data Noise as a Site-Specific Weight Parameter
952 in a Hierarchical Bayesian Moment Tensor Inversion: The Case Study of The Geysers

and Long Valley Caldera Earthquakes. *Bulletin of the Seismological Society of America*, ssabull;0120160379v1. https://doi.org/10.1785/0120160379

Mustać, M., Tkalčić, H., & Burky, A. L. (2018). The Variability and Interpretation of Earthquake Source Mechanisms in The Geysers Geothermal Field From a Bayesian Standpoint Based on the Choice of a Noise Model. *Journal of Geophysical Research: Solid Earth*, *123*(1), 513–532. https://doi.org/10.1002/2017JB014897

Mustać, M., Hejrani, B., Tkalčić, H., Kim, S., Lee, S.-J., & Cho, C.-S. (2020). Large Isotropic Component in the Source Mechanism of the 2013 Democratic People's Republic of Korea Nuclear Test Revealed via a Hierarchical Bayesian Inversion. *Bulletin of the Seismological Society of America*, *110*(1), 166–177. https://doi.org/10.1785/0120190062

Nakano, M., Kumagai, H., & Inoue, H. (2008). Waveform inversion in the frequency domain for the simultaneous determination of earthquake source mechanism and moment function. *Geophysical Journal International*, *173*(3), 1000–1011. https://doi.org/10.1111/j.1365-246X.2008.03783.x

Nettles, M., & Ekström, G. (1998). Faulting mechanism of anomalous earthquakes near Bárdarbunga Volcano, Iceland. *Journal of Geophysical Research: Solid Earth*, *103*(B8), 17973–17983. https://doi.org/10.1029/98JB01392

Pasyanos, M. E., & Chiang, A. (2021). Full Moment Tensor Solutions of U.S. Underground Nuclear Tests for Event Screening and Yield Estimation. *Bulletin of the Seismological Society of America*, *112*(1), 538–552. https://doi.org/10.1785/0120210167

Pasyanos, M. E., Dreger, D. S., & Romanowicz, B. (1996). Toward real-time estimation of regional moment tensors. *Bulletin of the Seismological Society of America*, *86*(5), 1255–1269. https://doi.org/10.1785/BSSA0860051255

Phạm, T.-S., & Tkalčić, H. (2021). Toward Improving Point-Source Moment-Tensor Inference by Incorporating 1D Earth Model's Uncertainty: Implications for the Long Valley Caldera Earthquakes. *Journal of Geophysical Research: Solid Earth*, *126*(11), e2021JB022477. https://doi.org/10.1029/2021JB022477

Piana Agostinetti, N., & Malinverno, A. (2010). Receiver function inversion by trans-dimensional Monte Carlo sampling. *Geophysical Journal International*, *181*(2), 858–872. https://doi.org/10.1111/j.1365-246X.2010.04530.x

Rögnvaldsson, S. Th., & Slunga, R. (1993). Routine fault plane solutions for local networks: A test with synthetic data. *Bulletin of the Seismological Society of America*, *83*(4), 1232–1247. https://doi.org/10.1785/BSSA0830041232

Romanowicz, B., Dreger, D., Pasyanos, M., & Uhrhammer, R. (1993). Monitoring of strain release in central and northern California using broadband data. *Geophysical Research Letters*, *20*(15), 1643–1646. https://doi.org/10.1029/93GL01540

Romanowicz, B. A. (1982). Moment tensor inversion of long period Rayleigh waves: A new approach. *Journal of Geophysical Research: Solid Earth*, *87*(B7), 5395–5407. https://doi.org/10.1029/JB087iB07p05395

992 Ross, A., Foulger, G. R., & Julian, B. R. (1996). Non-double-couple earthquake mechanisms at
993 the Geysers Geothermal Area, California. *Geophysical Research Letters*, *23*(8), 877–880.
994 https://doi.org/10.1029/96GL00590

995 Sambridge, M., Gallagher, K., Jackson, A., & Rickwood, P. (2006). Trans-dimensional inverse
996 problems, model comparison and the evidence. *Geophysical Journal International*,
997 *167*(2), 528–542. https://doi.org/10.1111/j.1365-246X.2006.03155.x

998 Sambridge, Malcolm. (1999). Geophysical inversion with a neighbourhood algorithm—II.
999 Appraising the ensemble. *Geophysical Journal International*, *138*(3), 727–746.
1000 https://doi.org/10.1046/j.1365-246x.1999.00900.x

1001 Sambridge, Malcolm, & Mosegaard, K. (2002). Monte Carlo Methods in Geophysical Inverse
1002 Problems. *Reviews of Geophysics*, *40*(3), 3-1-3–29.
1003 https://doi.org/10.1029/2000RG000089

1004 Saraò, A., Panza, G. F., Privitera, E., & Cocina, O. (2001). Non-double-couple mechanisms in
1005 the seismicity preceding the 1991-1993 Etna volcano eruption. *Geophysical Journal*
1006 *International*, *145*(2), 319–335. https://doi.org/10.1046/j.1365-246x.2001.01375.x

1007 Shang, X., & Tkalčić, H. (2020). Point-Source Inversion of Small and Moderate Earthquakes
1008 From P-wave Polarities and P/S Amplitude Ratios Within a Hierarchical Bayesian
1009 Framework: Implications for the Geysers Earthquakes. *Journal of Geophysical Research:*
1010 *Solid Earth*, *125*(2). https://doi.org/10.1029/2019JB018492

1011 Sipkin, S. A. (1986). Interpretation of non-double-couple earthquake mechanisms derived from
1012 moment tensor inversion. *Journal of Geophysical Research: Solid Earth*, *91*(B1), 531–
1013 547. https://doi.org/10.1029/JB091iB01p00531

1014 Staněk, F., Eisner, L., & Jan Moser, T. (2014). Stability of source mechanisms inverted from P-
1015 wave amplitude microseismic monitoring data acquired at the surface. *Geophysical*
1016 *Prospecting*, *62*(3), 475–490. https://doi.org/10.1111/1365-2478.12107

1017 Stump, B. W., & Johnson, L. R. (1977). The determination of source properties by the linear
1018 inversion of seismograms. *Bulletin of the Seismological Society of America*, *67*(6), 1489–
1019 1502. https://doi.org/10.1785/BSSA0670061489

1020 Tape, W., & Tape, C. (2012). A geometric setting for moment tensors: A geometric setting for
1021 moment tensors. *Geophysical Journal International*, *190*(1), 476–498.
1022 https://doi.org/10.1111/j.1365-246X.2012.05491.x

1023 Tarantola, A. (2005). *Inverse Problem Theory and Methods for Model Parameter Estimation*.
1024 Society for Industrial and Applied Mathematics.
1025 https://doi.org/10.1137/1.9780898717921

1026 Tarantola, A., & Valette, B. (1982). Inverse Problems = Quest for Information. *Journal of*
1027 *Geophysics*, 16.

1028 Tkalčić, H., Dreger, D. S., Foulger, G. R., & Julian, B. R. (2009). The Puzzle of the 1996
1029 Bardarbunga, Iceland, Earthquake: No Volumetric Component in the Source Mechanism.
1030 *Bulletin of the Seismological Society of America*, *99*(5), 3077–3085.
1031 https://doi.org/10.1785/0120080361

Tkalčić, Hrvoje, Kennett, B. L. N., & Cormier, V. F. (2009). On the inner-outer core density contrast from PKiKP/PcP amplitude ratios and uncertainties caused by seismic noise. *Geophysical Journal International*, *179*(1), 425–443. https://doi.org/10.1111/j.1365-246X.2009.04294.x

Vasyura-Bathke, H., Dettmer, J., Dutta, R., Mai, P. M., & Jónsson, S. (2021). Accounting for theory errors with empirical Bayesian noise models in nonlinear centroid moment tensor estimation. *Geophysical Journal International*, *225*(2), 1412–1431. https://doi.org/10.1093/gji/ggab034

Vavryčuk, V. (2001). Inversion for parameters of tensile earthquakes. *Journal of Geophysical Research: Solid Earth*, *106*(B8), 16339–16355. https://doi.org/10.1029/2001JB000372

Vavryčuk, V. (2011). Tensile earthquakes: Theory, modeling, and inversion. *Journal of Geophysical Research: Solid Earth*, *116*(B12). https://doi.org/10.1029/2011JB008770

Vavryčuk, V. (2015). Moment tensor decompositions revisited. *Journal of Seismology*, *19*(1), 231–252. https://doi.org/10.1007/s10950-014-9463-y

Vavryčuk, V., & Kühn, D. (2012). Moment tensor inversion of waveforms: a two-step time-frequency approach. *Geophysical Journal International*, *190*(3), 1761–1776. https://doi.org/10.1111/j.1365-246X.2012.05592.x

Wang, T., Shi, Q., Nikkhoo, M., Wei, S., Barbot, S., Dreger, D., et al. (2018). The rise, collapse, and compaction of Mt. Mantap from the 3 September 2017 North Korean nuclear test. *Science*, eaar7230. https://doi.org/10.1126/science.aar7230

Wang, X., & Zhan, Z. (2020). Moving from 1-D to 3-D velocity model: automated waveform-based earthquake moment tensor inversion in the Los Angeles region. *Geophysical Journal International*, *220*(1), 218–234. https://doi.org/10.1093/gji/ggz435

Xu, H., Ni, S., Liu, W., Zhu, H., & Wang, X. (2020). Focal mechanisms of the 2017 North Korean nuclear test and its early collapse event. *Geophysical Journal International*, *220*(2), 737–752. https://doi.org/10.1093/gji/ggz462

Yagi, Y., & Fukahata, Y. (2011). Introduction of uncertainty of Green's function into waveform inversion for seismic source processes: Uncertainty of Green's function in inversion. *Geophysical Journal International*, *186*(2), 711–720. https://doi.org/10.1111/j.1365-246X.2011.05043.x